The glial framework reveals white-matter fiber architecture in human and primate brains

Roey Schurr[1]*, Aviv A. Mezer[1]

5   [1]Edmond and Lily Safra Center for Brain Sciences, Hebrew University of Jerusalem; Jerusalem, Israel

*Corresponding author. Email: roey.schurr@mail.huji.ac.il

10

Uncovering the architecture of white-matter axons is fundamental to the study of brain networks. We developed a method for quantifying axonal orientations at ~15 micron resolution. This method is based on the common Nissl staining of postmortem histological slices. Nissl staining reveals the spatial organization of glial cells along axons. Using structure tensor analysis, we leveraged this patterned organization to uncover the local axonal orientation. We used Nissl-based structure-tensor analysis to extract fine details of axonal architecture and demonstrated its applicability in multiple datasets of humans and non-human primates. Nissl-based structure tensor analysis can be used to compare fine-grained features of axonal architecture across species, and is widely applicable to existing datasets.

5

One-Sentence Summary: Whole-brain glial cell organization provides a histological reference for axonal orientation across datasets and species.

10

A long-standing goal of neuroscience is the mapping of neural circuitry underlying cortical and subcortical computations (*1*, *2*). This entails mapping the axons that communicate information between brain regions. It is therefore essential to develop tools for fine-grained measurement of white-matter architecture at a cellular resolution. Existing methods are either limited to animal studies (*3*), require highly specialized equipment for data acquisition and processing (*4–8*), or require specialized stains for myelin, whose staining quality is highly sensitive to the exact staining procedure (*9*, *10*).

One of the most common tools for studying brain tissue postmortem is Nissl staining, which targets the cell nuclei. It has revolutionized our understanding of the cortical gray matter and has been used extensively to inform cortical parcellations based on cytoarchitectonic features (*11*). However, it has never been used to study the architecture of the white matter, which mostly comprises of axons and glial cells. This state of affairs has left the white matter as *terra incognita* in Nissl-based histological atlases.

We developed a method for visualizing and quantifying in-plane fiber orientations at a resolution of ~15 microns, based on postmortem histological slices stained for Nissl. To extract the fiber orientations, we utilize the spatial organization of glial cells within white matter. Studies of specific white-matter tracts have shown that astrocytes and myelinating oligodendrocytes cluster in short rows aligned with the axons that they support (12, 13). Such studies refer to this organization as the "glial framework" of the white matter.

We hypothesized that by measuring the local orientation glial cells across the white matter, we could infer the underlying axonal architecture. To measure the in-plane glial orientation we used structure tensor analysis, a technique from computational image processing often used for quantifying local orientations in textured images (*14*, *15*). The structure tensor is a matrix derived from the partial derivatives of the image intensity along the x and y axes (see Methods for mathematical formulation; (*16*)). The second eigenvector of this matrix points in the direction minimal changes in intensity values, i.e., along oriented structures such as glial rows in the Nissl-stained white matter. We applied structure tensor analysis to quantify the orientation of glial rows and to visualize the underlying fiber architecture. We term this technique "Nissl-based structure tensor" (Nissl-ST). We applied Nissl-ST to several independent datasets of humans and non-human primates.

First, we demonstrated the applicability of Nissl-ST in the human corpus callosum, the major white-matter tract that connects the two hemispheres. Fig. 1 shows that the stained cells tend to cluster in short rows, as predicted by the glial framework assumption (all figures are based on Dataset 1 unless stated otherwise). Remarkably, the orientation of these short rows is not arbitrary; rather, nearby rows are similarly oriented, and their orientation agrees with the known orientation of neighboring axons (*17*). The local orientations generally agree with the macroscopic orientation of the corpus callosum.

To increase signal-to-noise ratio in the pixel-wise ST calculation, we convolved each tensor element with a Gaussian smoothing kernel (with a standard deviation of $\rho=15$ microns) (*18*) (Fig. S1). Calculating the ST at every pixel (Fig. 1C) allowed us to construct a polar histogram summarizing the glial-rows orientation density function (gODF) in every image tile of 200^2 microns^2 (Fig. 1D). Hence, the measurement's effective spatial resolution is determined by the Gaussian kernel (15 microns) and the resolution of the tiles used for extracting peak orientations

(here we used tiles of 50^2 or 200^2 microns^2). As expected in the corpus callosum, where axons are coherently oriented, the gODFs are narrow and present a sharp peak (*17, 19*). Throughout this work, the vector field of peak orientation extracted from the gODF is presented in whole-slice, color-coded in-plane orientation maps.
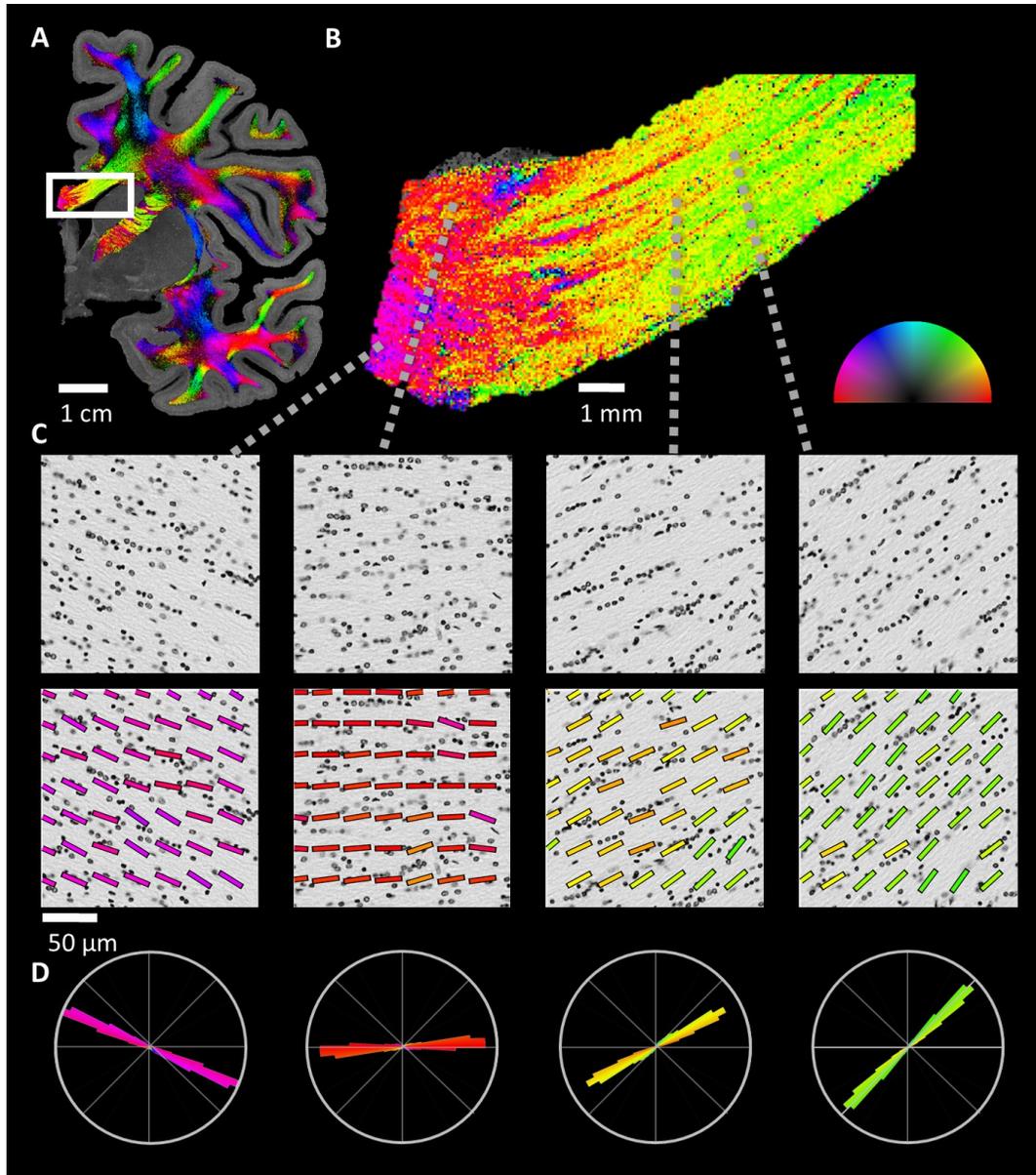
5

Fig. 1. Nissl-based structure tensor analysis of the human corpus callosum. *(**A**) In-plane orientation maps in a coronal slice of the right hemisphere (in tiles of 200^2 microns^2, smoothing kernel of 15 microns), color-coded according to the semicircle on the right. The in-plane orientation is calculated as the peak orientation of the structure tensors in each tile. (**B**) Magnified view of the corpus callosum (CC) region indicated in panel (a), calculated in 50×50 microns^2 tiles. (**C**) Example tiles from different locations along the CC. Top: Glial cells are organized in short rows oriented along nearby axons. Bottom: A subset of the pixel-wise orientations overlaid on top of the grayscale tiles. (**D**) Polar histograms of the glial-rows orientation distribution functions (gODF) in each tile.*

10

15

In Fig. 2 we compared the orientation map derived from Nissl-ST with a published image of postmortem polarized light imaging (PLI) (*20*) and with the orientation map derived from *in vivo* diffusion magnetic resonance imaging (MRI) (*21*, *22*). For the *in vivo* MRI data, the in-plane peak orientation was extracted from the spherical harmonics representation of the fiber orientation distribution function (ODF; see Methods and Fig. S2). At the macroscopic scale, all methods yield similar orientation maps, both in deep white matter and near the cortex, where many axons that enter or leave the cortex are oriented toward major gyral crowns. A closer look at several regions of interest revealed the fine details obtained with Nissl-ST and PLI. First, Nissl-ST captures the local incoherence of fibers in the corpus callosum (Fig. 2D, red and yellow tiles; (*17*)). It also reveals the fiber architecture known as Edinger's Comb (Fig. 2E), which is the crossing of the lenticular fasciculus (red) through the internal capsule (green) (*23*, *24*). Finally, Nissl-ST reveals fine fiber bundles such as the angular bundle (yellow), which connects the hippocampus and entorhinal cortex (Fig. 2F) (*25*). These fine details of the fiber architecture are captured with Nissl-ST and PLI, but are unresolved in the *in vivo* diffusion MRI, which is measured at a much lower resolution (1.25 mm isotropic).
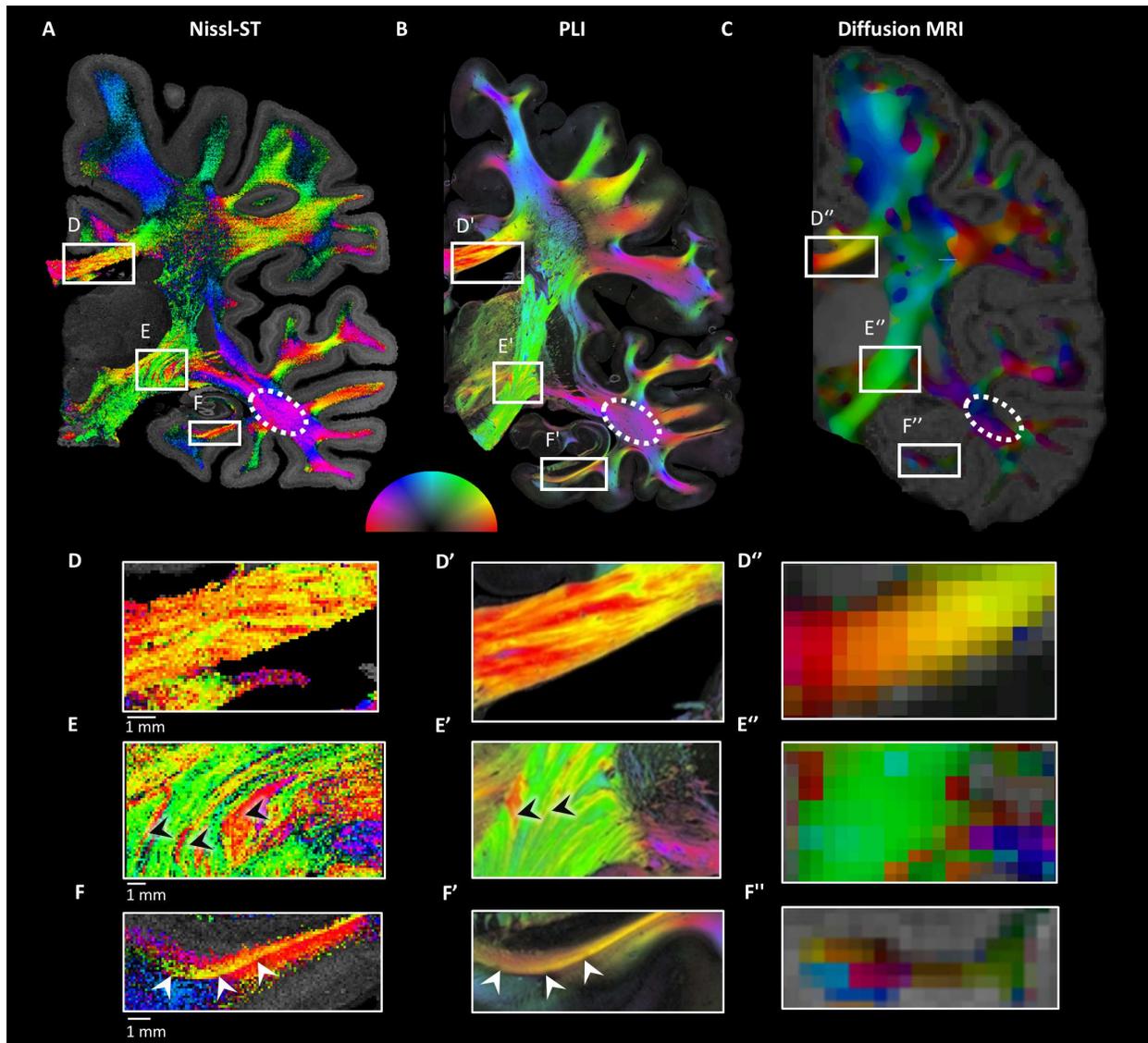
Fig. 2. Comparison of Nissl-based structure tensor and other methods. (A-C) *In-plane orientation maps in coronal slices of the right hemisphere from three different human datasets. **(A)** Nissl-based structure tensor (Nissl-ST, effective resolution ~15 microns, visualized with 200×200 microns² tiles), **(B)** polarized light imaging (PLI; in-plane resolution of 1.3×1.3 microns². Image reproduced with permission from Axer, Amunts et al., Forschungszentrum Jülich GmbH **(C)** in vivo diffusion MRI (resolution of 1.25 mm isotropic), showing peak-orientations projected onto the plane. To minimize sharp transitions in the more granular diffusion data, we smoothed the image using a median filter (see unsmoothed image in Fig. S3). All methods estimate similar orientations for the in-plane axons, even in regions where the predominant fiber bundle crosses perpendicular to the plane, such as the inferior longitudinal fasciculus (ILF, dashed ellipse; see Fig. S2) **(D-F)** Magnified views of the regions indicated in (A)-(C), visualized with 50×50 microns² tiles. **(D)** Local inhomogeneity in the corpus callosum. **(E)** Axons of the lenticular fasciculus (red, black arrowheads) that connect the subthalamic nucleus and the internal globus pallidus pass through the internal capsule (green), giving rise to the interchanging pattern of crossing fibers also known as Edinger's Comb. **(F)** The angular bundle (yellow, white arrowheads), which connects the hippocampus and entorhinal cortex.*

Next, we tested whether the glial framework persists in regions of axon crossing. Complex architectures such as axon crossing are ubiquitous in the brain, estimated to occur in 60-90% of white-matter voxels in a typical acquisition of diffusion MRI (*26*). To date, the glial framework has been explored in few studies, all of which focus on specific tracts in regions with a single fiber population (*13*, *27–29*). It is unknown how glial cells are distributed in in regions of axon crossing. Are they arranged in arrays of intersecting glial rows, or are they randomly distributed? This question has important biological implications (*28*): If the glial framework persists in regions of fiber crossing, this strengthens the assumption that the spatial organization of glial cells has functional implications, providing evidence that glial cells are tract-specific and are not shared across tracts. We found evidence supporting the persistence of the glial framework in regions of fiber crossing: First, our ability to obtain maps similar to those derived from PLI using only the Nissl-stained images suggested that the glial framework is a brain-wide feature. Second, a strong test case for the hypothesis that the glial framework persists in regions of fiber crossing is shown in regions in which the predominant orientation is of fibers that pass through the imaging plane. For example, the inferior longitudinal fasciculus (ILF) travels through the coronal plane and crosses fibers that enter the temporal lobe (Fig. 2, dashed ellipse; see Fig. S2 for the visualization of ILF orientation). If the glial framework broke in this fiber crossing, we would not expect to find a clear orientation in this region. However, we found a clear in-plane orientation originating from axons that cross the ILF (magenta). This in-plane orientation was also captured by PLI and *in vivo* diffusion MRI data. Hence, it seems that the glial cells that support in-plane axons that cross the ILF retain the spatial organization of short glial rows. These results suggest that the glial framework persists even in regions of axonal crossing.
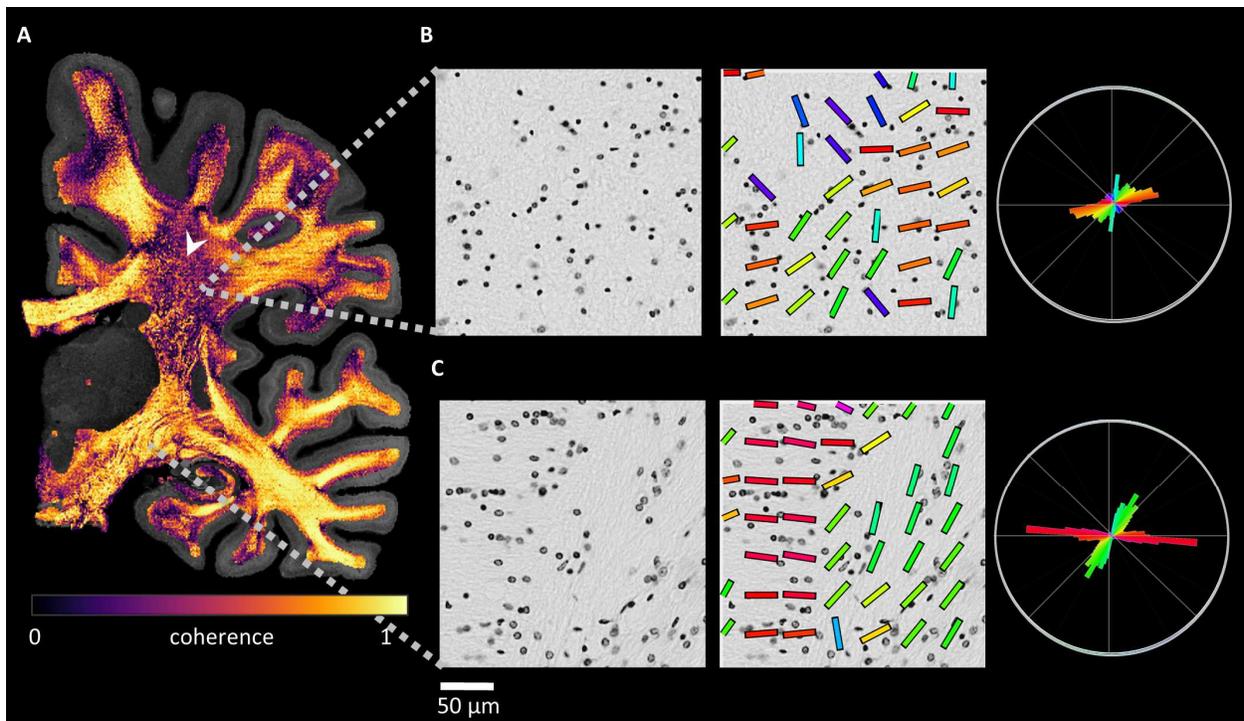

Fig. 3. Coherence of Nissl-based structure tensor across the brain. (A) *Coherence map of the in-plane orientation in the same slice as Fig. 2A. Low values indicate tiles of incoherent orientations, such as in the fiber-crossing region of the centrum semiovale (arrowhead).* ***(B)*** *Magnified view of a tile in a crossing region in the centrum semiovale. The incoherence is reflected in the isotropic*

gODF (right). **(C)** *Magnified view of a tile in the region of Edinger's Comb, where axons along the medial-lateral axis (red) cross axons along the inferior-superior axis (green). Crossing in this region manifests as a sharp change in the orientation of short glial rows.*

5   To further study the spatial organization of glial cells across the brain, we calculated how the coherence of in-plane orientation varies in space (Fig. 3A). The in-plane coherence quantifies the similarity between pixel-wise orientations across a region of interest. It is defined as the norm of the vector sum of all eigenvectors within the tile and ranges between 0 (incoherent orientations) and 1 (coherent orientations) (*30*). The coherence map in Fig. 3A reveals coherent regions both in
10 areas with known single-bundle populations (e.g., the corpus callosum) as well as in areas of in-plane axons that cross through-plane axons (e.g., the ILF). In contrast, the centrum semiovale, which is a three-way crossing region (*31*), shows low coherence values. To test whether Nissl-ST detects any prominent glial orientations in such regions of low coherence, we focused on the centrum semiovale and on Edinger's Comb. In the centrum semiovale we found less organized
15 spatial arrangement of glial cells compared with other regions, as reflected by the more isotropic gODF (Fig. 3B). This may be due, in part, to the limitation of Nissl-ST in recovering the orientation of through-plane axons. While Nissl-ST extracts a single orientation per pixel, the in-plane fiber crossing in this region can be evaluated over defined regions of interest (Fig. S4). The orientation of the through-plane crossing fibers remains unresolved due to the two-dimensional nature of
20 Nissl-ST. In the region of Edinger's Comb, two in-plane fiber bundles are intertwined, giving rise to a pattern of interchanging orientations (Fig. 3C). Close inspection of this region reveals a clear border between horizontal and vertical glial rows, which is evident also in the resulting two-peak gODF.

25 Regions of multiple fiber crossing may result in greater uncertainty in peak orientation. We quantified the uncertainty in peak orientation using a bootstrap approach. Uncertainty was typically low, with a 95% confidence interval ≤3° in 90% of the white-matter pixels (Fig. S5). Higher values of uncertainty were localized mostly to the centrum semiovale. Besides fiber crossing, we found that other potential sources of signal typically did not affect the peak orientation
30 extracted with Nissl-ST. These other sources include blood vessels (Fig. S6-7) as well as background fibrous structures (Fig. S8-9). While blood volume in the white matter is estimated to be only 2.57% (*32*), the estimated peak orientation could be affected in atypical regions with very high blood vessel volume (Fig. S7). Rare white-matter neurons probably do not affect the results of Nissl-ST, as even near the gray matter, where the fraction of white-matter neurons is higher
35 than in deep white matter (*33*), Nissl-ST provided useful orientation information (Fig. S10). See Supplementary Text for a detailed account of these analyses.

We further explored the effects of three non-biological sources also could affect the results of Nissl-ST: image resolution, imaging noise and staining variability. First, to test the effect of the
40 raw data's spatial resolution on Nissl-ST, we compared the estimated orientations in downsampled versions of the same data. We found that downsampling increased the angular difference with respect to the native-resolution image (Fig. S11; Sup. Table 1). Furthermore, an in-plane resolution lower than 5×5 microns^2 limited the accuracy of the recovered orientations, with a median angular difference of 15 degrees. Second, since Nissl-ST is based on computing image gradients, imaging
45 noise can negatively affect the orientation estimation (*16*). Qualitatively, visual inspection of the high-quality data we used here suggests that imaging noise is very low and unlikely to affect the results of Nissl-ST. Indeed, quantitatively, we found an extremely low level of imaging noise in these data, with a normalized variance smaller than 10^{-4} (see Methods). We performed simulations

in which we added higher levels of noise, and found that increasing levels of noise increased the angular error of Nissl-ST (though denoising methods can reduce the effects of severe noise; Table S2; Fig. S12-14). Finally, some nuclei may appear lighter than others in Nissl-stained slices, due either to actual variability in staining or to their different positions along the depth of the slice. We

5 simulated variable levels of cell staining and found that Nissl-ST is robust to staining variability (Fig. S15). See Supplementary Text for more details on these analyses.

An exciting application of the orientation maps derived from Nissl-ST is the digital reconstruction of white-matter pathways using existing histological datasets. Here, we used deterministic

10 tractography (*34*) over the peak in-plane orientations derived from Nissl-ST to reconstruct white-matter pathways in the human brain. Fig. S16 shows the reconstruction of the corpus callosum. In addition, we tested the ability of Nissl-ST to resolve short association fibers (U-fibers). We found that the high resolution of Nissl-ST allows the reconstruction of U-fibers, and provided evidence for a U-fiber system around the occipitotemporal sulcus. While the exact cortical endpoints of

15 reconstructed fibers can only be measured in axonal tracing studies, the ultra-high resolution of Nissl-ST can provide complementary information to existing techniques for U-fiber mapping (*5*, *35*) (see Supplementary Text).

To establish the wide applicability of Nissl-ST to multiple datasets and species, we applied it to

20 histological sections of four independent datasets: two human specimens (*36*, *37*) and two non-human primates (a rhesus macaque and a vervet monkey; available at http://brainmaps.org/). Fig. 4A shows the orientation maps derived from each dataset. Nissl-ST successfully extracted meaningful orientation maps with similar features across datasets. Furthermore, we found that the region of Edinger's Comb (white arrowhead) is conserved across species, showing a similar

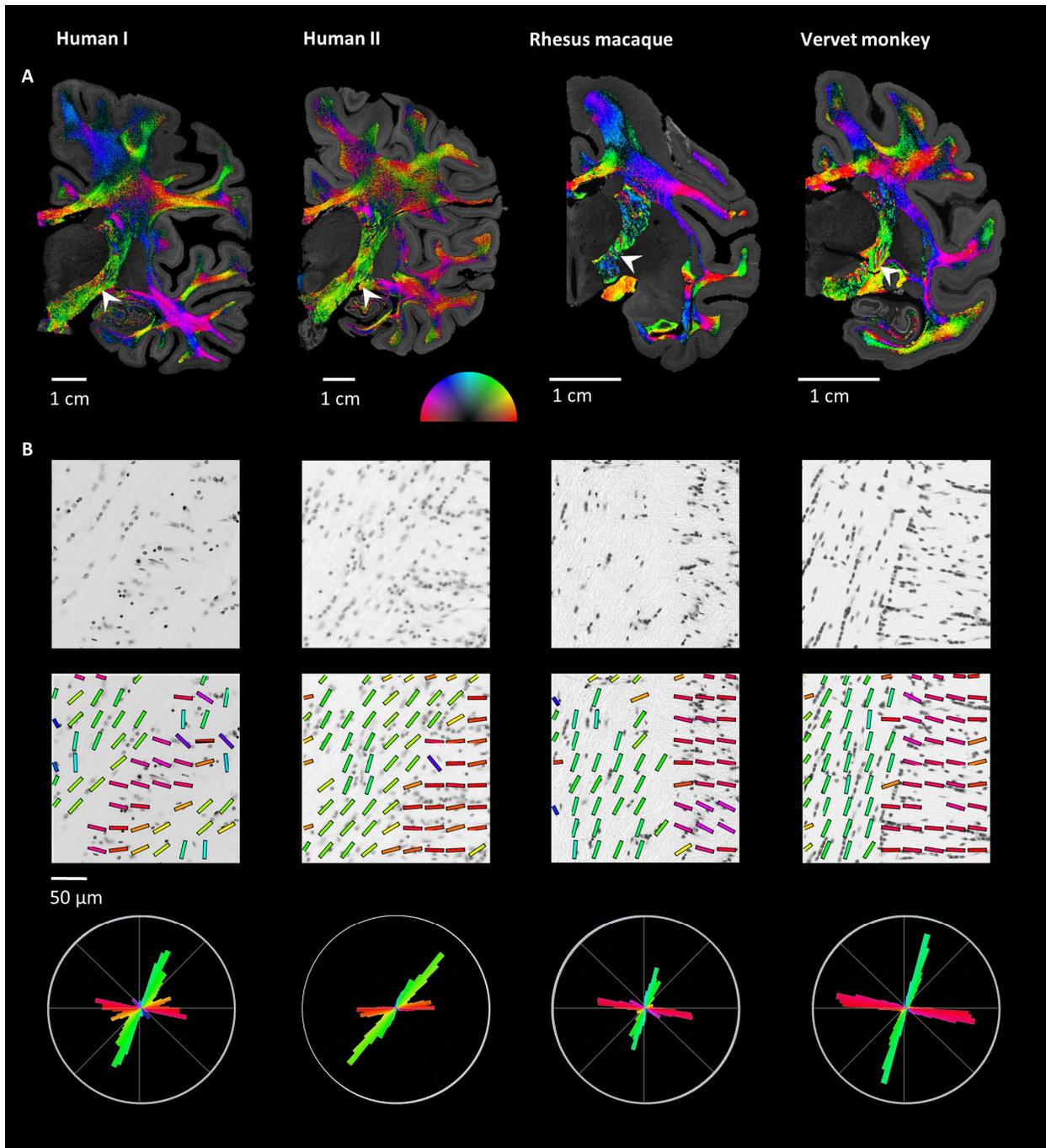25 characteristic crossing of glial rows in each specimen (Fig. 4B).

***Fig. 4. Applicability of Nissl-based structure tensor across datasets. (A)** In-plane orientation maps in coronal slices of four independent datasets, demonstrating the applicability of Nissl-ST to existing histological datasets of humans and non-human primates (rhesus macaque and vervet monkey), establishing the existence of the whole-brain glial framework across species. **(B)** A magnified view of tile from Edinger's Comb in each specimen (white arrowheads in (A)). The characteristic axonal crossing in this region is preserved across species.*

Nissl-ST has great potential for use in future studies of white matter in normal development, normal aging (*38*) and pathological states that affect the white matter, like schizophrenia (*39*).

Such applications of Nissl-ST will need to account for the unique challenges that the histological data may present. For example, pathological conditions accompanied by microglial response may be accompanied by an alternation to the spatial distribution of glial cells (*40*). Development, especially at prenatal stages, poses a fascinating challenge for Nissl-ST: On the one hand, Nissl-ST provides a potential means to study the initial development of myelin, as some studies in the rat found that already at birth, oligodendroglial progenitor cells are assembled in short rows that resemble those of the adult brain (*27*). On the other hand, since the relative proportion of different cell types changes in development (*41*, *42*), it is possible that at early stages of development, the main source of the signal in Nissl-ST would be other cell types (e.g., endothelial cells), thereby masking the effect of the short glial rows. To demonstrate applicability of Nissl-ST to developmental data, we compared the dataset of the adult rhesus macaque (Fig. 7) to 120 days embryonic stage and 14 days postnatal. These data suggest that at 120 embryonic days, the density of glial cells (or their progenitors) is very low compared with that of the 14 days postnatal brain (Fig. S17), with the latter much more similar to the adult case. Furthermore, at 120 embryonic days, the cells did not seem organized in short rows. In contrast, by 14 days postnatal, glial cells were already organized in short rows along the axons' expected orientation. Future research focusing on the intermediate stages in development therefore could shed light on the process and ordering of myelination across white-matter pathways.

A common feature of Nissl-ST, PLI and structure-tensor analysis based on myelin staining is their sensitivity to myelinated (rather than non-myelinated) axons. In addition, the proposed implementation of Nissl-ST is two-dimensional in nature. Hence, it is unable to resolve the orientation of through-plane fibers. Since glial cells associated with out-of-plane axons cannot be easily identified as such, they might introduce uncertainty into the method's orientation estimates. Future studies directly comparing Nissl-ST and PLI in the same slice could shed more light on their differential sensitivity to both in-plane and through-plane orientations. An exciting extension of the proposed technique would be generalizing the Nissl-ST method to three-dimensional datasets, such as the future high-resolution version of BigBrain (which used silver staining of cell bodies rather than Nissl staining (*43*)). Notably, this would require specialized tools for correcting between-section staining variability (*43*). Such three-dimensional datasets could be integrated with neuroimaging data using specially tailored toolboxes (*44*).

The glial framework — the patterned spatial organization of glial cells in the white matter — has been described in only a handful of pathways, namely the rat fimbria (*13*), the mouse corpus callosum (*28*) and the vervet corpus callosum (*29*). Additionally, Pandya and Schmahmann (2006) briefly mentioned the glial framework (which they call the "glial matrix") in the context of the ILF and the nearby tracts. It is a longstanding question whether the glial framework extends to all myelinated tracts, especially phylogenetically younger tracts. Here, we found direct evidence that this is the case for the corpus callosum, the lenticular fasciculus and the internal capsule in humans, rhesus macaques and vervet monkeys, as well as a U-fiber around the occipitotemporal sulcus in the human brain. The overall similarity of in-plane orientation maps derived from Nissl-ST and from PLI suggests that the structured organization of glial cells along axons extends to other white-matter tracts.

The model-free approach of Nissl-ST reveals a surprisingly rich layer of information in Nissl stained brain slices, which has been hitherto unused. An advantage of Nissl-ST compared with existing methods is the inherent coregistration of the novel maps that can be derived from white matter and the maps derived from cortical and subcortical structures. This would allow for an easy

integration of Nissl-based atlases of gray matter structures alongside maps of white-matter architecture. The abundance of Nissl stained resources in labs around the globe, as well as the prevalence of digitized datasets and open-source atlases including high-resolution Nissl stained slices (*36*, *37*, *45*, *46*) make the proposed technique readily applicable to numerous datasets. Importantly, such datasets would allow for the comparison of fine-grained features of fiber architecture across species as well as between healthy and diseased brains and would provide a simple way to obtain a histological reference for *in vivo* white-matter mapping.

5

References and Notes

1.   B. A. Wandell,. *Annu. Rev. Neurosci.* **39**, 103 (2016).

2.   H. Takemura, M. Thiebaut de Schotten, *Brain Struct. Funct.* **225** (2020), 1189.

3.   J. D. Schmahmann, D. N. Pandya, *Fiber Pathways of the Brain* (Oxford University Press, 2006).

4.   M. Axer et al., *Front. Neuroinform.* **5**, 34 (2011).

5.   H. Takemura et al., *Elife*. **9**, 1 (2020).

6.   J. Men et al., *IEEE J. Sel. Top. Quantum Electron.* **22**, 120 (2016).

7.   M. Menzel et al., *Neuroimage*. **233**, 117952 (2021).

8.   H. R. Ueda et al., *Nat. Rev. Neurosci.* **21, 61** (2020) .

9.   C. Stüber et al., *Neuroimage*. **93 Pt 1**, 95 (2014).

10.   A. Yendiki, M. Aggarwal, M. Axer, A. F. D. Howard, A.-M. van C. van Walsum, S. N. Haber, *bioRxiv*, (2021), doi:10.1101/2021.04.16.440223.

11.   K. Amunts, K. Zilles, *Neuron*. **88**, 1086 (2015).

12.   N. Baumann, D. Pham-Dinh, *Physiol. Rev.* **81**, 871 (2001).

13.   M. Suzuki, G. Raisman, *Glia*. **6**, 222 (1992).

14.   J. Bigun, G. H. Granlund, J. Wiklund, *IEEE Trans. Pattern Anal. Mach. Intell.* **13**, 775 (1991).

15.   M. D. Budde, J. A. Frank, *Neuroimage*. **63**, 1 (2012).

16.   W. Zhang, J. Fehrenbach, A. Desmaison, V. Lobjois, B. Ducommun, P. Weiss, *IEEE Trans. Med. Imaging*. **35**, 294 (2016).

17.   J. Mollink et al., *Neuroimage*. **157**, 561 (2017).

18.   R. M. Bourne et al., *NMR Biomed,* **32**, 1 (2019).

19.   M. D. Budde, J. Annese, *Front. Integr. Neurosci.* **7**, 3 (2013).

20.   K. Amunts, A. Lindner, K. Zilles, *e-Neuroforum*. **5**, 43 (2014).

21.   P. J. Basser, J. Mattiello, D. LeBihan, *J. Magn. Reson. B*. **103**, 247 (1994).

22.   J. D. Tournier, F. Calamante, D. G. Gadian, A. Connelly, *Neuroimage*. **23**, 1176 (2004).

23.   A. Horn et al., *Neurology*. **92** E1163 (2019).

24.   E. J. L. Alho et al., *Mov. Disord.* **35**, 75 (2020).

25.   M. M. Zeineh et al., *Cereb. Cortex*. **27**, 1779 (2017).

26.   B. Jeurissen, A. Leemans, J.-D. Tournier, D. K. Jones, J. Sijbers, *Hum. Brain Mapp.* **34**, 2747 (2013).

27.   R. Hardy, R. Reynolds, *J. Neurosci. Res.* **47**, 455 (1997).

28.   T. Tanaka, N. Ohno, Y. Osanai, S. Saitoh, T. Q. Thai, K. Nishimura et al., *Glia.* **69**, 2488 (2021).

29.   M. Andersson et al., *Proc. Natl. Acad. Sci. U. S. A.* **117**, 33649 (2021).

30.   J.-P. Lachaux, E. Rodriguez, J. Martinerie, F. J. Varela, *Hum. Brain Mapp.,* **8**, 194 (1999).

31.   K. Schilling, Y. Gao, V. Janve, I. Stepniewska, B. A. Landman, A. W. Anderson, *NMR Biomed.* **30**, e3787 (2017).

32.   J. Doucette, C. Kames, E. Hernández-Torres, A. Traboulsee, A. Rauscher, *bioRxiv*, (2019) doi:10.1101/614008.

33.   V. García-Marín, L. Blazquez-Llorca, J. R. Rodriguez, J. Gonzalez-Soriano, J. DeFelipe, *J. Comp. Neurol.* **518**, 4740 (2010).

34.   S. Mori, B. J. Crain, V. P. Chacko, P. C. M. Van Zijl, *Ann. Neurol.* **45**, 265 (1999).

35.   M. Guevara, P. Guevara, C. Román, J. F. Mangin, *Neuroimage*. **212**, 116673 (2020).

36.   J. K. Mai, M. Majtanik, G. Paxinos, *Atlas of the Human Brain* (Academic Press, Amsterdam, ed. 4, 2015).

37.   J. A. Miller et al., *Nature*. **508**, 199 (2014).

38.   J. D. Yeatman, B. A. Wandell, A. A. Mezer, *Nat. Commun.* **5**, 4932 (2014).

39.   J. Fitzsimmons, M. Kubicki, M. E. Shenton, *Curr. Opin. Psychiatry*. **26**, 172 (2013).

40.   S. Hickman, S. Izzy, P. Sen, L. Morsett, J. El Khoury, *Nat. Neurosci.* **21**, 1359 (2018).

41.   R. R. Sturrock, *J. Anat.* **122**, 521 (1976).

42.   R. K. Sigaard, M. Kjær, B. Pakkenberg, *Cereb. Cortex*. **26**, 89 (2016).

43.   K. Amunts et al., *Science* **340**, 1472–1475 (2013).

44.   C. Paquola et al. *bioRxiv*, (2021), doi:10.1101/2021.05.04.442563.
45.   S. Mikula, I. Trotts, J. M. Stone, E. G. Jones, *Neuroimage*. **35**, 9 (2007).
46.   G. Striedter, The Zoomable Human Brain Atlas Website, (available at https://zoomablebrain.bio.uci.edu/).

5

Authors contributions: Conceptualization, methodology, formal analysis, visualization and writing; RS and AAM. Supervision: AAM.
Competing interests: The authors declare no competing interests.
Data and materials availability: All original datasets used in this work can be accessed on the websites listed in the Methods section. The MATLAB code for calculating and visualizing the structure tensor is available together with code for downloading example data at https://github.com/MezerLab/NisslST. Fig. S18 shows the expected outputs of the example code.

Science

AAAS

Supplementary Materials for

The glial framework reveals white-matter fiber architecture in human and primate brains

Roey Schurr, Aviv A. Mezer

Correspondence to: roey.schurr@mail.huji.ac.il

This PDF file includes:

Materials and Methods
Supplementary Text
Table S1-S2
Fig S1-S19
References (47-70)

Materials and Methods

Datasets

We used four datasets of postmortem coronal brain sections stained with Nissl staining. Two datasets were from human donors, and two from non-human primates, as described below.

Dataset 1 is part of the Atlas of the Human Brain in Stereotaxic (MNI) Space. It consists of coronal slices from the right hemisphere of a 26-year-old male from the Vogt collection of Düsseldorf. Full details regarding the tissue and its histological processing can be found at Atlas of the Human Brain ((*36*); Section 2.1 Material and Methods). In short, the brain was fixed in formalin three hours after the time of death. The brain then was cut into five vertically oriented blocks and embedded in paraffin, and later sliced into 20-micron-thick coronal slices. 50 slices were stained using cresyl violet or hematoxylin. All slices were photographed at 0.645x0.645 microns^2 resolution in-plane and can be viewed online at www.thehumanbrain.info. Here, we used slices r3-1373 (Fig. 1), r3-0570 (Fig. 2, Fig. 3) and r3-0720 (Fig. 4).

Dataset 2 is part of the BrainSpan Atlas of the Developing Human Brain Project (*37*). It consists of coronal sections from the left hemisphere of a 34-year-old woman. Full details regarding the tissue and its histological processing can be found in the Reference Atlases Documentation at: http://help.brain-map.org/display/humanbrain/Documentation. In short, the brain was fixed in formalin three hours after the time of death. The brain was cut into eight approximately vertically oriented blocks and embedded in paraffin, and later sliced into 20-micron-thick coronal slices. All slices were photographed at 0.97^2 microns^2 resolution in-plane and are available online at http://atlas.brain-map.org. Here, we used slice 112360921 (Fig. 4).

Datasets 3 and 4 are part of the BrainMaps (*47*) brain atlas. Dataset 3 consists of a coronal section from the brain of an adult rhesus macaque (*Macaca mulatta*; dataset ID 159). The brain was frozen and sliced into 30-micron-thick coronal slices. All slices were photographed at 0.46x0.46 microns^2 resolution in-plane and are available on-line at http://brainmaps.org/. Here, we used slice 400 (Fig. 4).

Dataset 4 consists of a coronal section from the brain of an adult vervet monkey (*Chlorocebus aethiops*; dataset ID 42). The brain was embedded in gelatin and sliced into 40-micron-thick coronal slices. All slices were photographed at 0.46x0.46 microns^2 resolution in-plane and are available online at http://brainmaps.org/. Here, we used slice 207 (Fig. 4).

Datasets 5 and 6 are part of the NIH Blueprint Non-Human Primate (NHP) Atlas, which is available online at http://atlas.brain-map.org. Dataset 5 consists of a coronal section from the brain of a prenatal male rhesus macaque (*Macaca mulatta*; dataset ID 121051250), at embryonic day 120. The brain was frozen and sliced into 50-micron-thick coronal slices. All slices were photographed at 0.97×0.97 microns^2 resolution in-plane. Here, we used slice 127838348.

Dataset 6 consists of a coronal section from the brain of a neonate male rhesus macaque (dataset ID 112192062), at 14 days postnatal. The brain was frozen and sliced into 50-micron-thick coronal slices. All slices were photographed at 0.97x0.97 microns^2 resolution in-plane. Here, we used slice 112352912.

Structure tensor analysis

To assess the local orientation of short glial rows, we used structure tensor analysis (15, 48, 49), based on the MATLAB implementation of (16). The structure tensor is often used in image texture analysis and crucially does not require the segmentation of individual cells. Instead, the structure tensor is calculated based on the partial derivatives of the image (see below). We converted each histological image to grayscale and calculated the structure tensor for each pixel using MATLAB (MathWorks, Natwick, MI, USA), with the code provided in the paper of (16). Given a grayscale image I, the structure tensor J is defined as the matrix of partial derivatives of the image, $I_x = \frac{dI}{dx}$ and $I_y = \frac{dI}{dy}$:

$$J = \begin{pmatrix} \langle I_x, I_x \rangle_w & \langle I_x, I_y \rangle_w \\ \langle I_x, I_y \rangle_w & \langle I_y, I_y \rangle_w \end{pmatrix}$$

where $\langle f, g \rangle_w$ denotes the weighted inner product of two images f, g, with a Gaussian smoothing kernel $w(x, y)$. The width of the kernel w, denoted by ρ, defines the local neighborhood over which the tensor is calculated. Following (18), we used a Gaussian kernel with a standard deviation of ρ=15 microns. For each pixel, we extracted the orientation of the eigenvector associated with the smallest eigenvalue of the structure tensor (the orientation of minimal changes in intensity values, i.e., along oriented structures). Visual inspection revealed that in Dataset 2 (human brain) results were improved in terms of agreement with other datasets, if the image is smoothed first. We therefore smoothed the image of Dataset 2 with a Gaussian smoothing kernel of σ=3 microns prior to calculating the structure tensor.

To visualize the results, we divided each slice into tiles of size 200^2 microns^2. For zoomed-in visualization, we used tiles of 50^2 microns^2. For each tile, we calculated the distribution of local orientations and then extracted the peak orientation. To minimize the contribution of pixels far from any stained cell (farther than the standard deviation of the smoothing kernel, ρ), we created a pixel inclusion mask as follows: We binarized each tile using the Otsu threshold (50) with MATLAB's "graythresh" function, and included only those pixels that were as close as ρ to any glial cell pixel. We visualized the glial-row orientation distribution function (gODF) using a polar histogram with a bin width of 3 degrees.

To calculate the meso-scale anisotropy, we calculated the coherence of pixel-wise orientations in each tile. The coherence is defined as the norm of the vector sum of all eigenvectors within the tile (30). Coherence ranges between 0 (incoherent orientation) and 1 (coherent orientations), and can be thought of as a measure similar to the fractional anisotropy (FA) in diffusion MRI (51).

We present the orientational information as color-coded maps (15) restricted to the white matter, and overlaid on a grayscale image of the mean intensity in each tile. The RGB value is determined by the peak orientation, and shaded by the coherence value of the tile.

For visualization of the white-matter orientation maps, we generated a white-matter mask at the level of 200^2 microns^2 tiles. We generated the white-matter mask based on a whole-slice image with a high contrast between gray- and white-matter, which we constructed as follows. First, we binarized each image tile. Then, we identified connected components within the binary image, using MATLAB's "bwconncomp" with default parameters. Then, we calculated the 95th percentile

size of connected components in each tile. This yielded a whole-slice image with a high contrast between white- and gray-matter, reflecting the fact that the white matter contains smaller connected components compared with the gray matter (Fig. S18). To generate the initial white-matter mask, we binarized this whole-slice image using Otsu's method and filled in holes in the resulting mask. We further corrected the white-matter mask by manual inspection.

Certainty measures of peak orientation

We used a nonparametric bootstrap approach to estimate the certainty of the peak orientation calculated with Nissl-ST. For every 200^2 microns^2 tile in a coronal slice from Dataset 1 we calculated the peak orientation 500 times. Each time we randomly sampled the pixel-wise orientations (with repeats), and calculated the peak orientation. We used the 95% confidence interval as a measure of the certainty in peak orientation.

The effect of biological sources on Nissl-ST

The effect of blood vessels

To study the effect of blood vessels on the results of Nissl-ST, we used a coronal slice from Dataset 1 and manually chose 500^2 microns^2 tiles that include blood vessels. We applied Nissl-ST and visualized the local orientations throughout the entire tile. To study the differential contribution of blood vessels to Nissl-ST, we repeated the Nissl-ST analysis after manually segmenting and removing the blood vessels, which we performed using GIMP's clone tool (*52*).

The effect of background fibrous structures

To test whether the orientation of Nissl-ST is driven by background fibrous structures, we removed the fibrous structures by binarizing the histological image, and the repeated the Nissl-ST analysis. Specifically, we binarized every 200^2 microns^2 tile in a coronal slice from Dataset 1 using an Otsu threshold. Since stained nuclei are much darker than the fibrous structures, applying the Otsu threshold resulted in the complete removal of fibrous structures in the background (Fig. S8). We applied Nissl-ST to the binarized images and calculated the peak orientation. We calculated the angular difference of the resulting orientations with respect to those extracted from the original image.

Peak orientations near cortical gray matter

To examine the ability of Nissl-ST to recover peak orientations as axons approach or leave the cortical gray matter (GM), we used a coronal slice from Dataset 1 and focused on the superior frontal gyrus. First, we applied a histogram equalization to the high-resolution histological image, in order to increase the contrast between white matter (WM) and GM. Then, we manually traced the border of the WM. Even at such a high resolution, it is impossible to determine the GM/WM border precisely, and instead we observed a gradual transition from WM to GM. Therefore, we defined the GM/WM border as the band of 200 microns at the end of the WM.

In Nissl staining, one can identify glial cells and neurons based on their distinct cytological features (*53*). To support our definition of the GM/WM border, we quantified the neuronal density in each tissue type (GM, WM, and GM/WM border). We used the ilastik toolkit ((*54*); www.ilastik.org), which allows the user to train machine-learning tools to perform different image analysis tasks. We used the Pixel Classification workflow and trained a random-forest classifier based on pixel-level features to separate the stained cells from the background. The classifier further classified cells as either glial cells or neurons. By counting the number of connected components in the

image, whose pixels were classified as neurons, we obtained a gross estimate of the density of neurons (neurons/micron^2) within each tissue type.

We applied Nissl-ST to particularly small 50^2 microns^2 tiles within the WM and GM/WM border regions and calculated the orientation distribution functions in both tissue types.

The effect of non-biological sources on Nissl-ST

Spatial resolution analysis

To study the effect of spatial resolution on the quantification of local orientation, we used a single human brain slice from Dataset 1. Starting with the native in-plane resolution of 0.645^2 microns^2, we downsampled the histological image by five different factors (2, 4 8, 16, and 32), yielding an effective in-plane resolution of approximately 1.3^2, 2.6^2, 5.2^2, 10.3^2 and 20.6^2 microns^2, respectively. We calculated the structure tensor analysis as above, and extracted the peak orientation in each 200^2 microns^2 tile. For each downsampling factor, we calculated the angular difference with respect to the peak orientation from the higher, native resolution. Here we assumed that the higher resolutions yield more accurate orientations and that a large difference between the orientation derived from original and downsampled images is a sign of low stability and plausible erroneous orientation estimates.

Robustness to noise

To assess the robustness of Nissl-ST to imaging noise, we used a coronal slice of a human brain from Dataset 1. First, we verified that the data we used does not suffer from imaging noise. For this aim, we derived an empirical estimation of the noise-level in the data: From the slice image, we extracted a background region that contained no tissue. We divided the pixel values by 255 to obtain a normalized image with values in the range 0 (black) and 1 (white). Assuming that this background region should have uniform intensity values, we define the normalized noise variance as the variance of the gray-level values across this large region of interest (*55*).

To assess the robustness of Nissl-ST to imaging noise in possibly noise-corrupted datasets, first we focused on the corpus callosum of Dataset 1, using a 200^2 microns^2 tile. We normalized the grayscale image to the range of 0-1 and used MATLAB's "imnoise" function to add Gaussian noise with mean 0 and three values of variance (0.05, 0.50 and 1.00, which are more than two orders of magnitude larger than the empirically estimated noise in the data). For each variance value, we generated 1,000 noisy images. We further denoised each noise-corrupted image either using a simple Gaussian filter using MATLAB's "imgaussfilt" with a smoothing kernel of 2 pixels, or using the Block-matching and 3D filtering (BM3D) package implemented in MATLAB (*56*). For each of the 1,000 repeats, we applied Nissl-ST to extract the peak orientation from the noisy and the two denoised images, and calculated the angular error of the peak orientation with respect to the original grayscale image.

To further study how the sensitivity to noise changes across the slice, we introduced Gaussian noise to the entire coronal slice. Here, we chose used a normalized noise variance of 0.05 and 0.2. Since our preliminary analysis on the region of the corpus callosum showed no advantage of BM3D over Gaussian filtering, here we denoised the image using a Gaussian filter. We applied Nissl-ST to extract the peak orientations and calculate the angular error of the peak orientation with respect to the original grayscale image.

Robustness to staining variability

To test the robustness of Nissl-ST to staining variability (resulting either from true staining variability or from the position of each cell within the depth of the histological slice), we used two 200^2 microns^2 tiles from the corpus callosum of Dataset 1. We binarized each image and further applied a watershed algorithm to separate contiguous cells. Using each binarized image, we simulated images of variable staining as follows: For each cell, we randomly chose a gray-level value from a uniform distribution in the range of 127±30. In addition to this between-cell variability, we simulated a sub-population of lightly stained cells as follows. We randomly chose a predetermined fraction of the cells and scaled their gray-scale level by a factor of 5 to result in lighter shades of gray (Fig. S15). We repeated this for 0, 10, 20, 30, 40 or 50% of the cells. For each predetermined fraction, we generated 1,000 simulated images and applied Nissl-ST to extract the peak orientation. For each repeat, we calculated the angular error of the peak orientation with respect to the original binary image.

Tractography using Nissl-ST

To test whether the vector field of peak orientations from Nissl-ST can be used to reconstruct white-matter pathways in the brain, we used a coronal slice from Dataset 1. We focused on two white-matter pathways: the corpus callosum and a U-fiber around the occipitotemporal sulcus (OTS). First, we converted the Nissl-ST-based peak orientations to NIfTI format. We used the NIfTI as input to a deterministic tractography algorithm called Fiber Assigned by Continuous Tracking (FACT; (*34*)), which we implemented with MRtrix3. We used a step size of 2 microns and a maximal angle of 60° between successive steps. Streamlines were seeded in seed regions of interest in the white matter (Fig. S16A, inset). In each pixel we seeded 5 streamlines. Tracking was terminated when streamlines left the white-matter mask. Streamlines were visualized using the Automatic Fiber Quantification toolbox (*57*).

In vivo diffusion MRI

To compare the results of Nissl-ST with *in vivo* diffusion MRI, we used the data of subject 100307 from the publicly available Human Connectome Project (HCP (*58*)). We downloaded the data that had been processed using the HCP preprocessing pipeline (*59*). The diffusion-weighted MRI data consisted of 90 noncollinear diffusion-weighted directions with a b-value of 2000 s/mm^2, and six non-diffusion-weighted images with a b-value of 0 s/mm^2, with a resolution of 1.25 mm isotropic. The anatomical T1-weighted image had a resolution of 0.7 mm isotropic.

We calculated the in-plane peak orientation in a coronal slice using the constrained spherical deconvolution (CSD) method as implemented by MRtrix 3.0 (*60, 61*). We resampled the resulting spherical fiber orientation distributions to the resolution of the anatomical data (0.7 mm). From each voxel we extracted the largest two peak orientations of fibers using the MRTrix functions fod2fixel and fixel2voxel (*62*). We projected each peak onto the coronal plane and then calculated its in-plane orientation. To extract a single in-plane orientation for each voxel, we used the following procedure: For each peak we calculated the apparent fiber density (AFD (*63*)) and the orientation with respect to the coronal plane. By default, we chose the peak associated with the greatest AFD. We chose the second peak only in voxels where the second peak had a larger projection onto the coronal plane, and also exceeded a threshold of 0.2 times the maximal AFD in the voxel (to minimize the inclusion of noisy peaks). This yielded a single in-plane orientation for each voxel, based on the CSD model of the diffusion data. To minimize sharp transitions due to choosing a single peak per voxel, we smoothed the in-plane orientation map using a median filter with a radius of 2 voxels (see Fig. S3 for comparing the smoothed and unsmoothed images).

Polarized light imaging

The PLI image in Fig. 2 was kindly provided by Axer, Amunts et al., Forschungszentrum Jülich GmbH. It is of a human donor, and was scanned at a spatial resolution of 1.3x1.3 microns^2 in-plane, and a slice thickness of 60 microns.

5

Supplementary Text
Throughout this work, we provide strong evidence that Nissl-ST can recover local fiber orientations by leveraging the glial framework. Here, we describe complementary analyses that support the utility of Nissl-ST and explore the potential effects of various biological and imaging sources that could contribute to the Nissl-ST signal.

The effect of biological sources on Nissl-ST

<u>The effect of blood vessels</u>

Nissl staining is not specific to the glial cells of the glial framework. Hence, other stained structures, such as blood vessels, also might affect the peak orientation, which then would make them a confounding factor. Indeed, Nissl also stains the endothelial cells that line the blood vessels, making it challenging to eliminate their contribution to Nissl-ST. However, previous studies have estimated the total blood volume in the white matter to be only 2.57% (*32*). The same study found that one-third of the blood resides in blood vessels parallel to white-matter tracts. (Others reported similar findings (*64, 65*)). Consequently, only a fraction of the blood vessels could negatively affect the recovered orientations. Other studies also have noted that the density of blood vessels in white matter is significantly smaller compared with cortical and subcortical gray matter (*65*).

To study the effect of blood vessels in our data, we manually identified image tiles that include blood vessels within the white matter in a coronal slice of a human brain from Dataset 1. Blood vessels were identified by their unique appearance: stained nuclei of endothelial cells that line the blood vessel are often elongated and assume the tubular shape of the blood capillaries (*53*). We found that Nissl-ST captures the local orientations of the blood vessels, but due to the relatively low density of blood vessels, they likely do not affect the extracted peak orientations substantially. In Fig. S6A we identify blood vessels that have the same orientation as the glia network, and in Fig. S6B and S7 we show blood vessels that are orthogonal to the glia network but do not contribute to the calculated orientation due to their low density. In Fig. S7C we select a smaller tile within Fig. S7A in which a blood vessel occupies a large fraction of the image. In this unique case, an erroneous peak orientation occurs (although it is still smaller compared to the peak orientation in this particular tile).

In an additional analysis, we manually removed the blood vessels from the same images. We applied Nissl-ST and extracted the local and peak orientations again. We found that the peak orientations in all these images were unchanged (Fig. S6-7).

We note that care must be taken in analyzing datasets of early embryonic specimens, in which endothelial cells may comprise a larger fraction of white-matter cells (see Fig. S17). A complete elimination of blood-vessel effects would require specialized techniques, such as a specialized staining designed for identifying vasculature or an automatic segmentation method for identifying blood vessels using machine-learning techniques.

<u>The effect of background fibrous structures</u>

A close inspection of the histological sections reveals a biological source that may contribute to Nissl-ST: background fibrous structures, which are most likely axons (e.g., Fig. 1C, Fig. 4B). To verify that these background fibrous structures are not the main source of the signal in the Nissl-ST orientations, we removed them by binarizing the image and leaving only stained cell nuclei (Fig. S8; see Methods). In the 200^2 microns^2 tiles from the corpus callosum that we used in Fig. S8, we found an angular difference of 1-4° between binary and grayscale images. At the whole-

slice level, we found that the resulting orientation map is very similar to that of the original image (median angular difference of 8°), with high angular differences localized mostly in the region of the centrum semiovale (Fig. S9). These results suggest that while the background fibrous structures may contribute some information to Nissl-ST, they are not the main source of the signal in Nissl-ST analysis.

White-matter neurons and peak orientations near cortical gray matter
Another potential biological source of signal for Nissl-ST is white-matter neurons. In the deep white matter, neurons comprise less than 1% of the cells (*66*) and are unlikely to affect the extracted orientations. While others have reported up to four times more neurons in the superficial white matter compared with deep white matter (*33*) this is still a small fraction of the cells compared with glial cells. Indeed, our tractography reconstruction of U-fibers based on Nissl-ST (Fig. S16) suggests that such rare neurons (also known as "solitary neurons") do not have a strong effect on the recovered orientations.

The observation that oligodendrocytes often are arranged in short rows even in the deep layers of the cortex (*53*) suggests that Nissl-ST could provide useful orientation information even for those axons that are close to the cortex. To investigate the applicability of Nissl-ST near cortical gray matter (GM), we focused on the superior temporal gyrus in a coronal section of a human brain from Dataset 1 (Fig. S10A-B). We manually traced the white-matter (WM) border, and defined the GM/WM border as the 200-micron-wide band extending from the GM into the WM. To support our definition of the GM/WM border, we calculated a gross estimate of the neuronal density within each tissue type (Fig. S10C-E; see Methods). Fig. S10D and S10E show a heatmap of the neurons' areal density and a summary bar plot, respectively. The results clearly demonstrate a very low density in the WM (median±median absolute deviation from the median (MAD) 0 ± 0 neurons/micron^2); a greater density in the GM/WM border (0.0004 ± 0.0004 neurons/micron^2); and the greatest density in the cortical GM (0.0008 ± 0.0004 neurons/micron^2).

To gain adequate sensitivity to local effects near the GM, we applied Nissl-ST in small tiles of 50^2 microns^2. Visual inspection of the resulting peak-orientation map in Fig. S10F reveals a general orientational preference towards the gyral crown (green). Typically, we did not observe a sharp transition to random orientations closer to the GM, suggesting that Nissl-ST provides useful information even in the GM/WM border region. Interestingly, in the lower part of the gyrus we observed tiles with less ordered orientations at the GM/WM border (Sup. Fig 10F-G, two arrowheads). We attribute this to the convoluted three-dimensional structure of the cortex and adjacent white matter in this region: As evidenced by the seemingly much thicker cortex in this region, this part of the gyrus is probably a region where the cortex folds obliquely with respect to the coronal histological section.

The effect of non-biological sources on Nissl-ST
In addition to the biological sources described above, we explored non-biological sources that could affect the results of Nissl-ST. First, we note that Nissl-ST, like other postmortem methods, may be compromised by staining artifacts or tears in the tissue. Such artifacts might manifest as large deviations in peak orientations over a small region, which would require visual inspection of the tissue in the affected regions. However, for the datasets we used here, the smoothness of the in-plane orientation maps suggests that such artifacts did not have a large effect. Below we discuss in detail the potential effects of other non-biological sources that could affect Nissl-ST – imaging noise and staining variability.

The effect of imaging noise

Imaging noise is expected to negatively affect the orientation estimation of Nissl-ST since it might change the local gradients that Nissl-ST is sensitive to (*16*). We estimated the imaging noise empirically by calculating the signal variance in a non-tissue region, which should have a uniform signal in the ideal case of no noise. First, we normalized the image grayscale levels to the range of 0 (black) and 1 (white). We found an extremely low level of imaging noise in these data, with a normalized signal variance smaller than 10^{-4} (see Methods). This is a very low level of noise compared to the relevant contrast in the image: The difference between the gray-levels of stained cells (0.3) and background tissue (0.8) is 0.5, three orders of magnitude larger than the noise variance. This suggests that imaging noise is not a limiting factor in these data.

Next, we used simulations to test the performance of Nissl-ST in the presence of greater imaging noise and to study the effects of image-denoising techniques. First, we focused on an image tile from the human corpus callosum (Fig. S12), and added mild (normalized noise variance of 0.05), severe (0.50) and extreme (1.00) levels of noise. Then we applied Nissl-ST to the noisy image and to denoised versions of the image. Fig S12 and Table S2 show that increasing levels of noise increased the angular error. Interestingly, while image denoising alleviated the effects of noise in the severe and extreme levels of noise, it showed no advantage in the case of mild noise, in which Gaussian denoising actually increased the angular error. This is likely because Gaussian denoising also introduces unwanted smoothing that affects the local image gradients. Under severe and extreme levels of noise, the advanced denoising technique (BM3D) and the simple Gaussian denoising yielded similar results.

Next, we studied the effects of noise across an entire coronal slice. Since BM3D showed no advantage over Gaussian denoising in the previous analysis, here we focused on Gaussian denoising. We added either mild (normalized noise variance of 0.05) or sever (0.20) levels of noise to the image. We found that the effect of noise varied across the slice, with greater noise sensitivity outside the corpus callosum (Fig. S13-14). Again, we found that denoising is advantageous only when severe (but not mild) noise has been added: With the addition of mild noise the median angular error across the slice was 8°, and increased to 10° after Gaussian denoising. In contrast, with the addition of severe noise, the median angular error across the slice was 21°, and dropped to 12° after Gaussian denoising. These results suggest that researchers who want to perform Nissl-ST analysis should first estimate their imaging noise, and should perform image denoising only if the estimated noise level is high.

The effect of staining variability

In Nissl-stained slices, some nuclei may appear lighter than others. Such variability could result either from actual variability in staining or from different cell positions along the depth of the slice. To explore the robustness of Nissl-ST to staining variability, we simulated variable levels of cell staining. We found that Nissl-ST is robust to staining variability (Fig. S15): Even when we simulate 50% lightly-stained cells, we found an angular difference of up to 3±2° (median±MAD) compared with an image of uniformly stained cells.

Tractography using Nissl-ST

Nissl-ST allows for the estimation of local fiber orientations at ultra-high (~15 microns) resolution. One potential application of Nissl-ST is the reconstruction of white-matter pathways in existing Nissl-stained datasets, in which little or no attention has been given to the white-matter. We

demonstrate tractography reconstructions based on Nissl-ST in two pathways in the human brain: the corpus callosum and a short association fiber (U-fiber) around the occipitotemporal sulcus (OTS).

5   Fig. S16 shows the reconstructions of the two pathways using deterministic tractography (*34*). The corpus callosum streamlines were seeded near the midline, and reach the superior frontal gyrus and the cingulate gyrus. Callosal fibers reaching the cingulate cortex are usually not reported in human studies, possibly due to the limitations diffusion MRI tractography (*67*). However, axonal tracing studies in the macaque have demonstrated that such callosal fibers do reach the cingulate

10   cortex (*3*). We also report a novel evidence for a U-fiber around the human OTS (Fig. S16). While the histological data that we use here cannot be used to dismiss the possibility that this putative U-fiber in fact represents axons that leave the inferior longitudinal fasciculus (ILF), we note that tract tracing studies have found direct connections between the gyri surrounding the OTS (reference (*3*), Plate 97). A similar U-fiber can be seen in a PLI study of the vervet monkey ((*5*), Fig. 7), and

15   possibly in a diffusion MRI study of the human brain as well (*68*).

We note that even at high resolutions such as those used here, the inherent limitations of tractography persists. For example, using deterministic tractography, the lateral projections of the corpus callosum cannot be reconstructed (*67*). Hence, while ultra-high resolution tractography

20   based on Nissl-ST is useful in complementing conventional diffusion MRI tractography studies and postmortem dissections studies, it cannot replace the ground-truth provided by axonal tracing studies, which are only feasible in animal studies.

Future studies could explore the use of probabilistic tractography algorithms based on Nissl-ST as

25   well. Such an analysis would require the extraction of multiple orientations per tile (or voxel), for example using bootstrap analysis, or by modelling the distribution of local orientations (e.g., with a mixture of von Mises distributions (*69*)). While existing datasets currently allow only 2-dimensional reconstructions, future datasets such as the upcoming 1-micron-resolution BigBrain (*70*) might allow for 3-dimensional reconstructions of fiber pathways.

30

Supplementary Tables

	DS=2	DS=4	DS=8	DS=16	DS=32
Effective pixel size [microns]	1.29	2.58	5.16	10.32	20.64
Median angular error	5°	10°	15°	20°	31°

Table S1. The effect of in-plane image resolution on the peak orientation. A coronal slice from Dataset 1 was analyzed with different downsampling (DS) factors. The median angular error with respect to the native resolution was calculated across the entire white matter. See Fig. S11.

	Mild (σ^2=0.05)	Severe (σ^2=0.50)	Extreme (σ^2=1.00)
Noisy	3±2°	19±12°	30±20°
Gaussian filter	7±2°	7±4°	10±6°
BM3D	3±2°	11±4°	10±4°

Table S2. The effect of imaging noise on the peak orientation in an image from the human corpus callosum. Angular errors in the form of median±median absolute deviation from the median (MAD) calculated over 1,000 repeats are shown for each image type across mild, severe and extreme noise values (σ^2 is the normalized noise variance). See Fig. S12.

Supplementary Figures
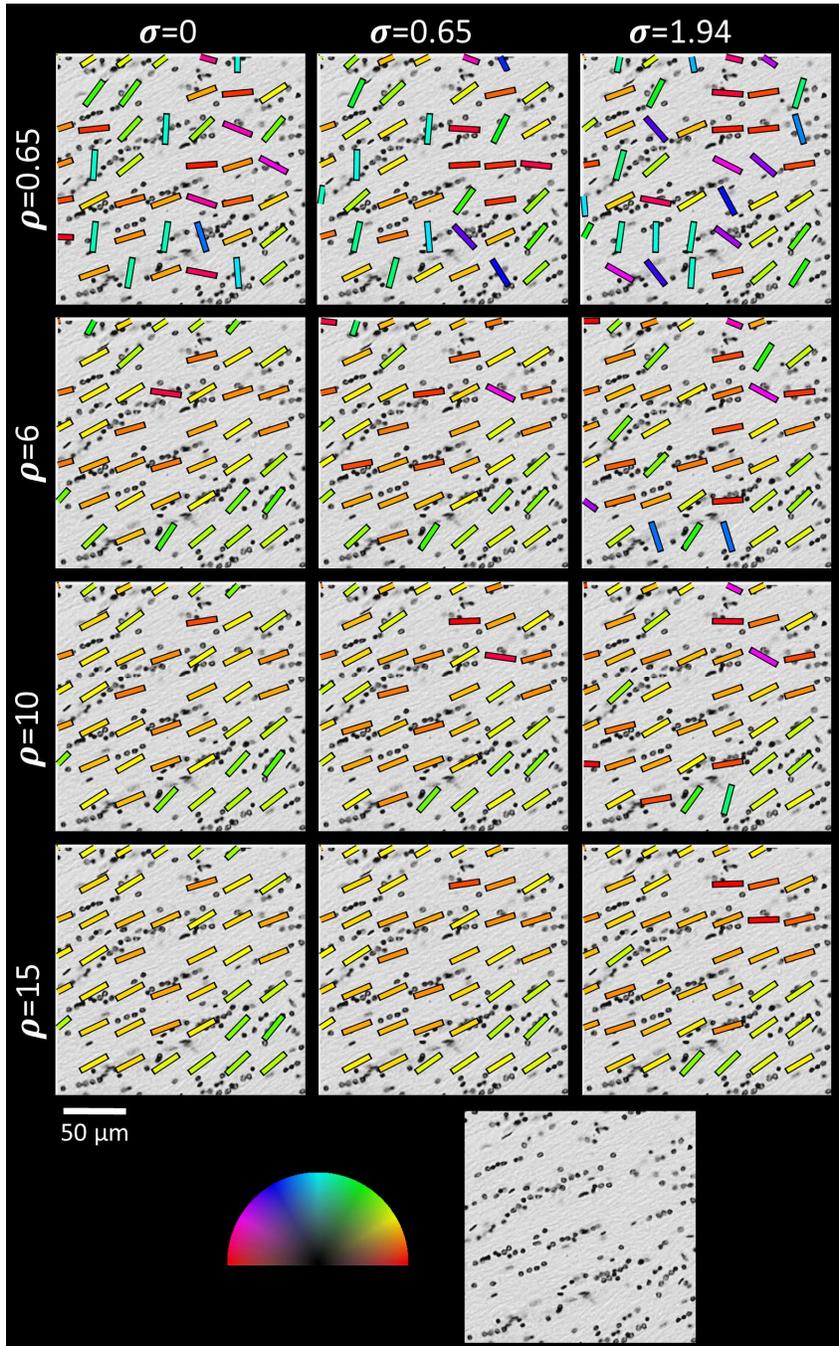
Fig. S1. The effect of algorithm parameters on the Nissl-based structure tensor. Each image shows the Nissl-based structure tensors of the same tile (bottom row) from Dataset 1. Here, the effect of ρ (the width of the Gaussian kernel for spatial regularization) is greater than the effect of σ (the width of the Gaussian smoothing kernel used to smooth the image before calculating the structure tensors). A possible explanation for the greater effect of ρ is that the larger Gaussian kernel of ρ leads to a regularization effect between the relatively distant neighboring rows. ρ and σ are given in microns. The main analysis was performed with σ=0 and ρ=15.
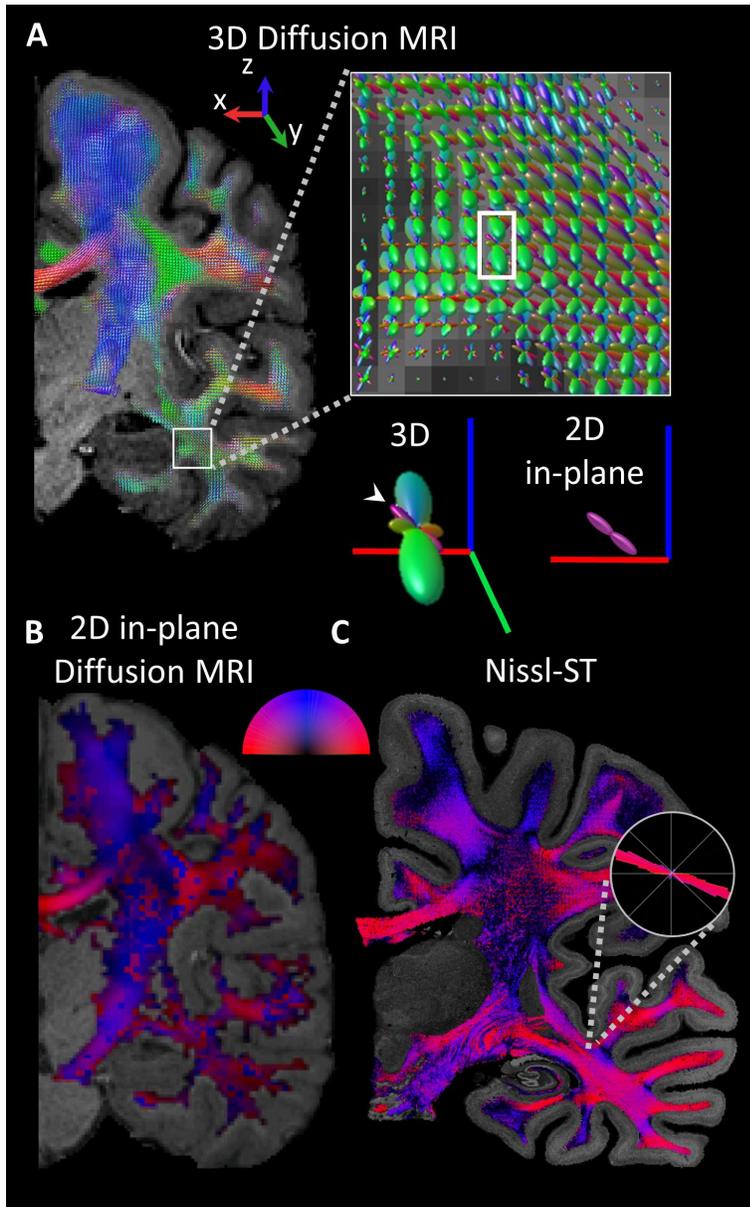
Fig. S2. Extracting in-plane orientations in regions of fiber crossing. (A) 3D fiber orientation distribution functions (fODFs) estimated from in vivo diffusion MRI using CSD (red: medial-lateral; green: anterior-posterior; blue: inferior-superior). **Inset**: Magnified view of the temporal lobe. The predominant fiber tract in this region is the interior longitudinal fasciculus (ILF, green) that passes through the plane. Fiber crossing the ILF is represented by secondary peaks in the fODF. **Bottom**: Magnified view of the fODF indicated above. The secondary in-plane peak (magenta) is marked by a white arrowhead. By projecting it to the coronal plane (right), the in-plane peak orientation can be extracted. **(B)** The in-plane peak orientation of the diffusion MRI data. Colormap as above, excluding the anterior-posterior axis (green). **(C)** Color-coded orientation map based on Nissl-ST. Inset: the gODF from a 200-micron tile in the region of the ILF and crossing fibers.
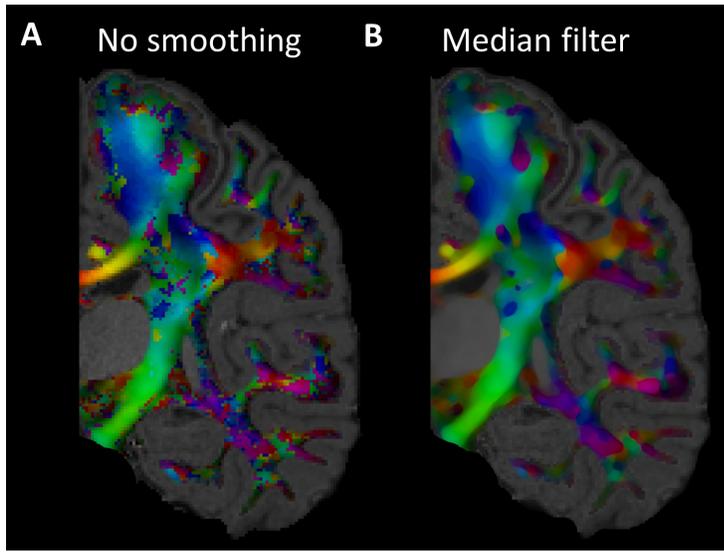
Fig. S3. Smoothing of the diffusion MRI in-plane orientation map. (A) The original in-plane orientation map. **(B)** The in-plane orientation map after smoothing with a median filter of two voxels.

5
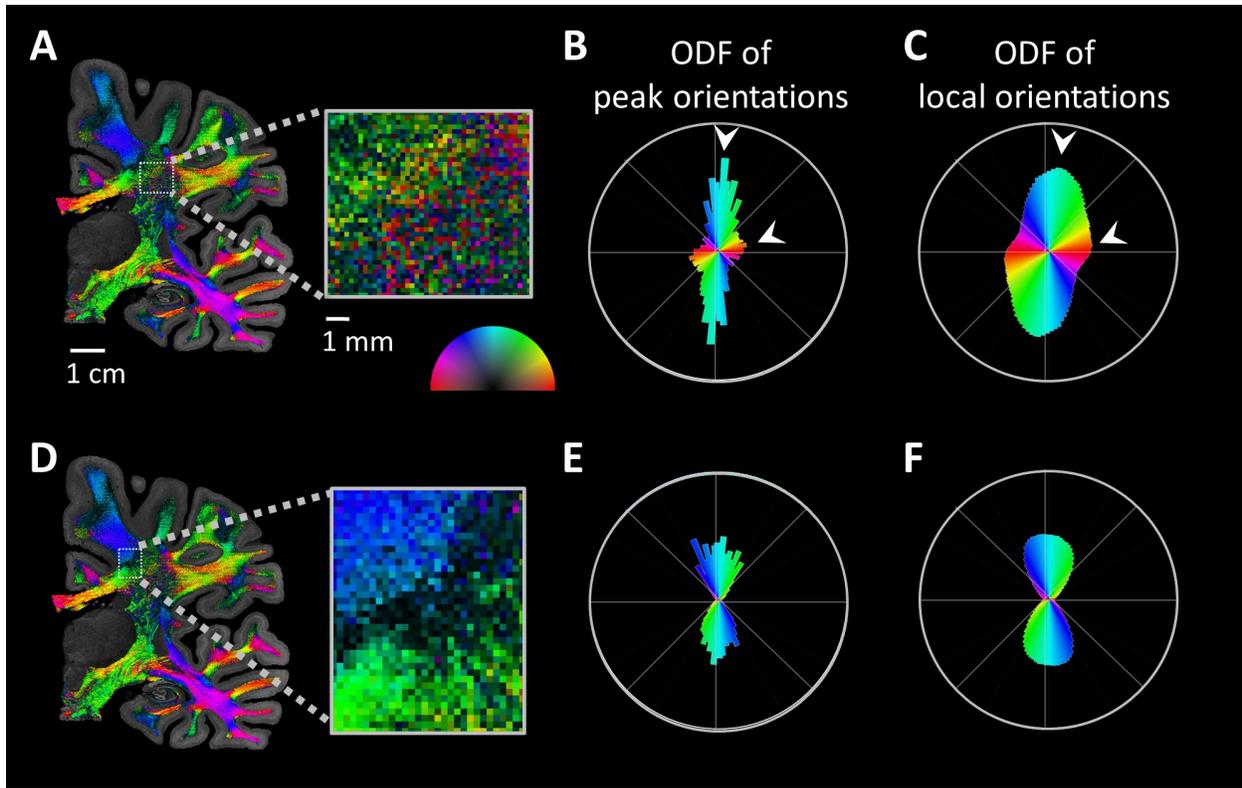
Fig. S4. Fiber crossing around the centrum semiovale. (A) In-plane orientation map in a coronal slice of the right hemisphere in tiles of 200^2 microns^2, color-coded according to the semicircle shown on the right. Inset shows a magnified view of the centrum semiovale, a known region of fiber crossing. **(B)** To visualize the fiber crossing in this region, we pooled the peak orientation across all inset tiles, and plotted the polar histogram of peak orientation (also known as the orientation distribution function or ODF). The histogram shows two prominent peaks, one vertical and one horizontal (white arrowheads). **(C)** The same peaks can be seen even without extracting the peak orientation in each tile (white arrowheads). Here, the polar histogram summarized all the local (pixel-wise) orientations in the inset. **(D)** The same slice as in (A), with a magnified region showing the corpus callosum (green) and the corona radiata (blue). **(E-F)** Polar histogram of the peak orientations **(E)** and all local orientations **(F)** in the ROI. Histograms show both diagonal (green and blue) and vertical (light blue) orientations.
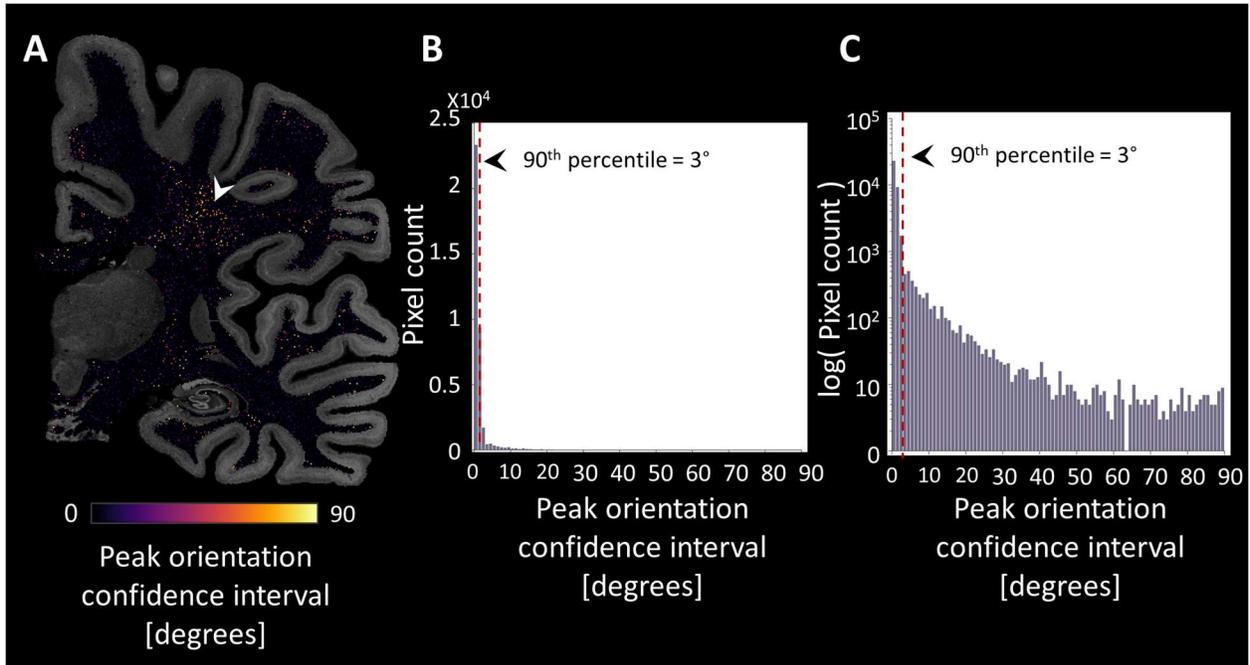
Fig. S5.
Confidence interval of the peak orientation. We computed the uncertainty of the peak orientations calculated with Nissl-ST using a nonparametric bootstrap approach. For every 200^2 microns^2 tile we calculated the peak orientation 500 times. Each time we randomly sampled the pixel-wise orientations (with repeats), and calculated the peak orientation. We used the 95% confidence interval as a measure of the certainty in peak orientation. **(A)** Heatmap of the bootstrap peak-orientation confidence interval. Higher values are found mostly in the region of the centrum semiovale. **(B)** Histogram of the confidence interval extracted from the entire white matter. The peak orientation is largely stable across the slice, with a 90th percentile of 3 degrees confidence interval (dashed red line). **(C)** The same histogram, with the y-axis in log scale.
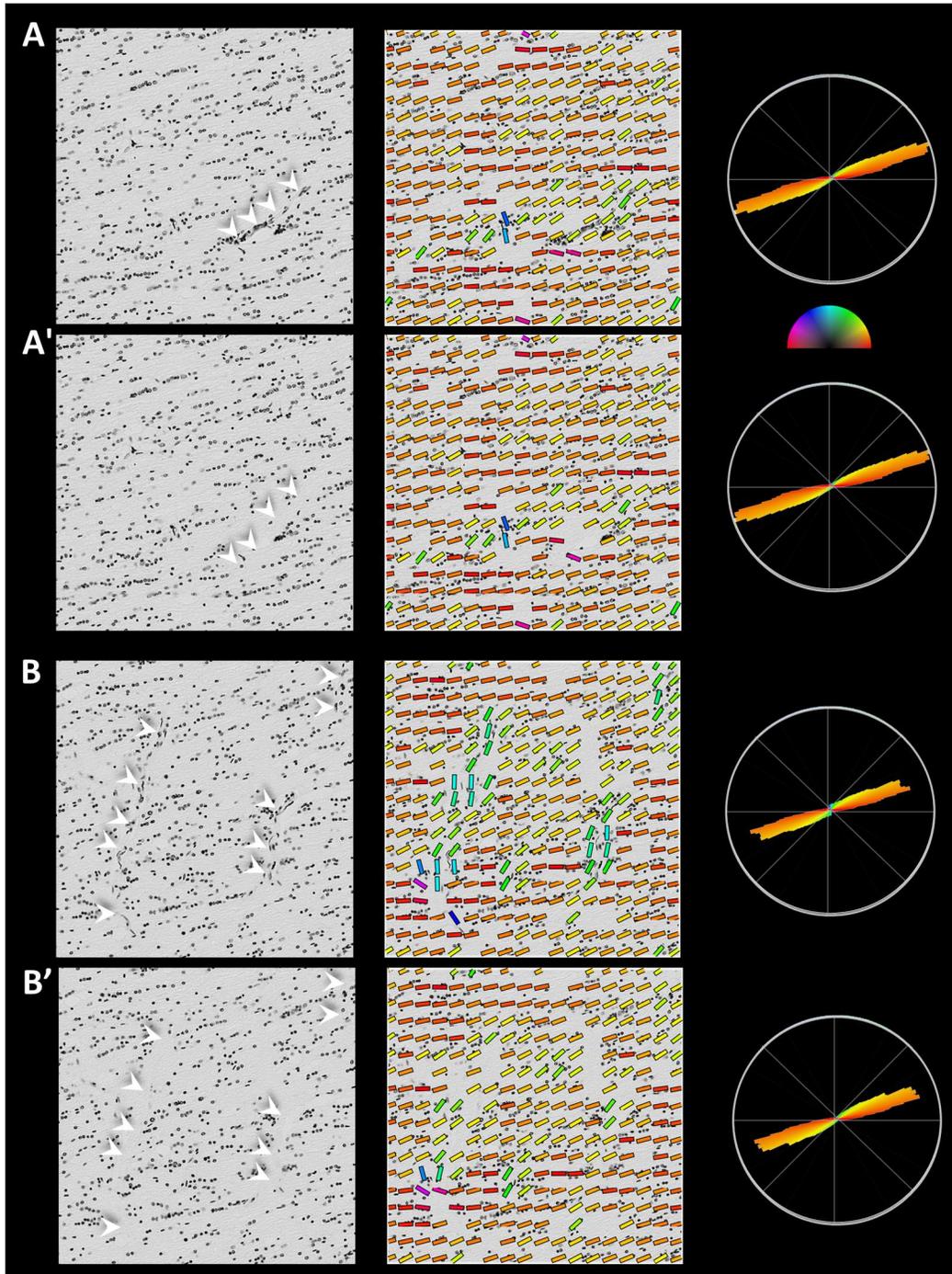
Fig. S6.
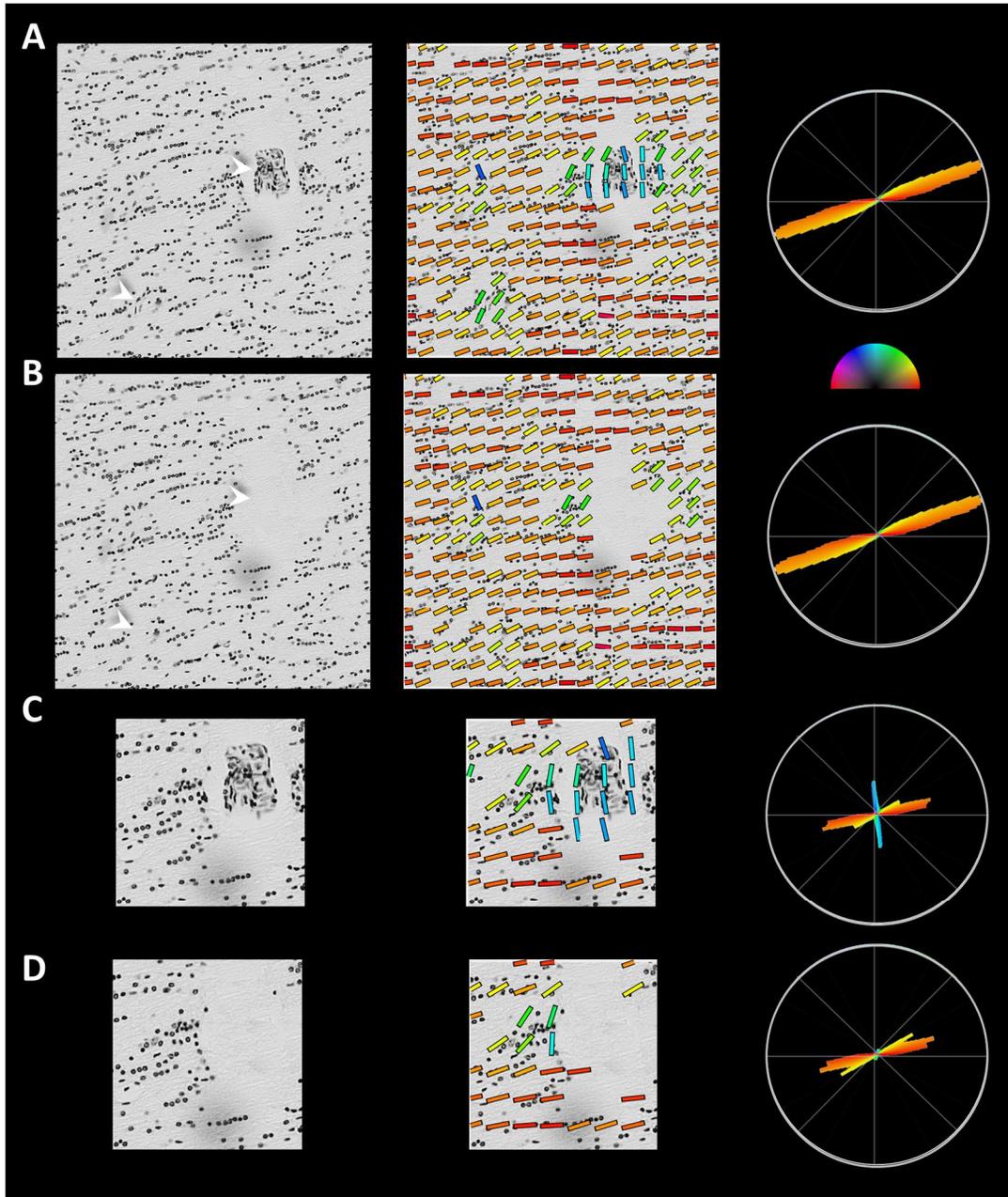**The effect of blood vessels on peak orientation. (A-B) Two** 500^2 microns^2 tiles from a coronal section of the corpus callosum, manually chosen to include blood vessels (white arrowheads). The stained nuclei of endothelial cells that line the blood vessel are often elongated and assume the tubular shape of the blood capillaries (*53*). In **(A)** and **(B)** the blood vessels are left intact, while in (**a'**) and (**b'**) they have been removed manually using the clone tool in GIMP. **Middle:** A subset of the pixel-wise orientations overlaid on top of the grayscale tiles. Blood vessels affect the local orientation estimate (green-blue). However, due to their low density, the blood vessels do not affect the peak orientation, as can be seen in the polar histogram of all pixel-wise orientations (**Right**).

Fig. S7.
The effect of blood vessels on peak orientation. (A) Left: A 500^2 microns^2 tile from a coronal section of the corpus callosum, manually chosen to include blood vessels (white arrowheads). The stained nuclei of endothelial cells that line the blood vessel are often elongated and assume the tubular shape of the blood capillaries (*53*). **Middle:** a subset of the pixel-wise orientations overlaid on top of the grayscale tiles. Blood vessels affect the local orientation estimate (green-blue). However, due to their low density, the blood vessels do not affect the peak orientation, as can be seen in the polar histogram of all pixel-wise orientations (**Right**). **(B)** The same slice as in panel (a), but with the blood vessels manually removed using the clone tool in GIMP. **(C-D)** Magnified view of the blood vessel region in (a-b). When the blood vessel takes up a large portion of the image, as in this example, it can affect the extracted peak orientation. Here, the polar histogram shows two prominent peaks: the main peak (orange) relates to the short glial rows orientation, and the secondary peak (cyan) is a spurious peak related to the blood vessels.
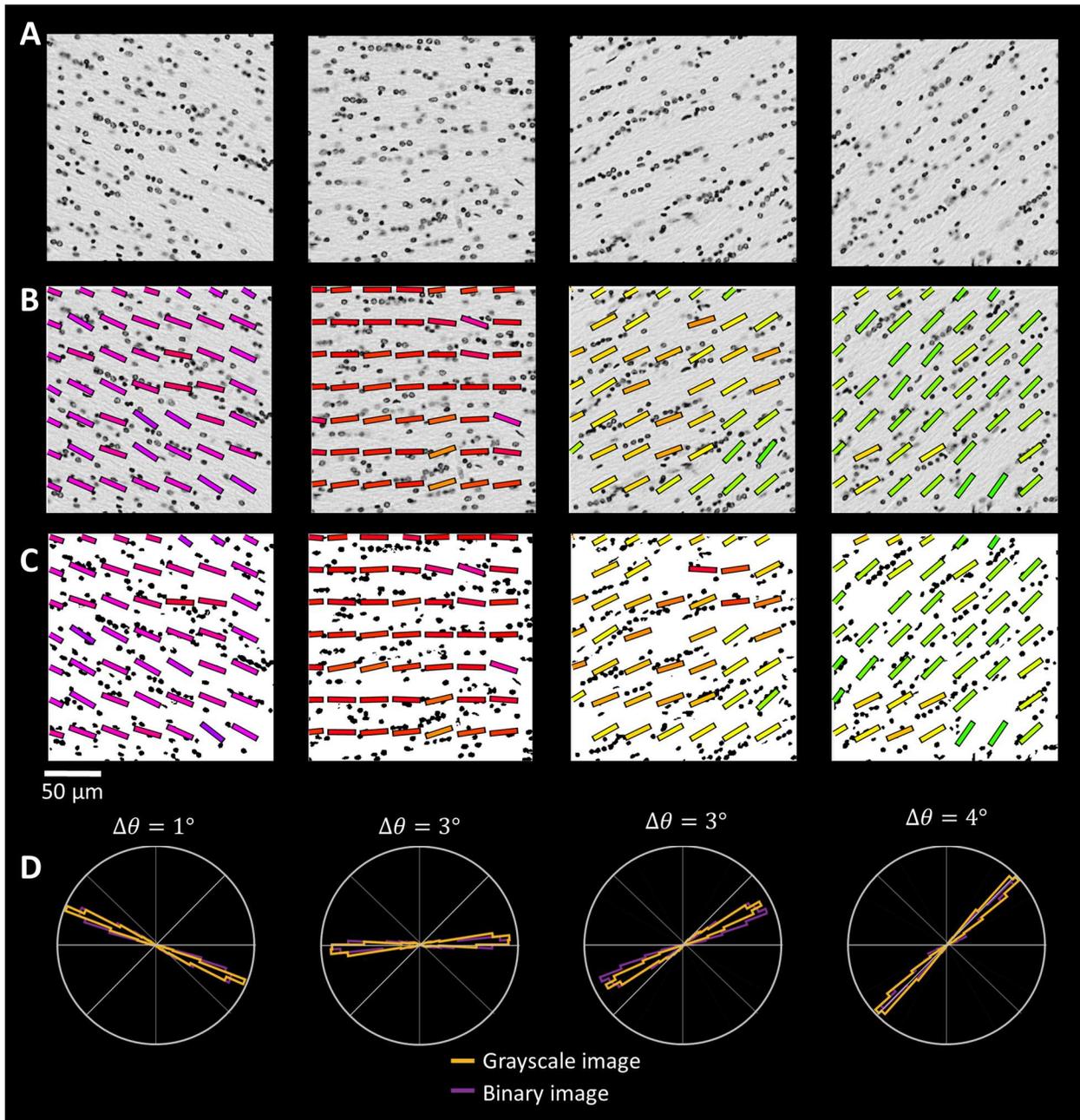
Fig. S8.

The effect of background fibrous structures on the peak orientation. (A) Four 200^2 microns^2 tiles from the corpus callosum (same as in Fig. 1). Fibrous structures, presumably the underlying axons, can be seen in each tile, orientated similarly to the glial rows. **(B)** A subset of the pixel-wise orientations overlaid on top of the grayscale tiles. **(C)** To remove the effect of background fibrous structures, each tile was binarized before applying Nissl-ST. Importantly, the local orientations are very similar between binarized (C) and non-binarized (B) images. **(D)** Polar histograms showing the glial-rows orientation distribution functions (gODF) in each tile, for the grayscale (yellow) and the binarized (purple) images. The peak orientation differs only slightly, as indicated by the values of Δθ above each histogram. See Fig. S9 for whole-slice analysis.
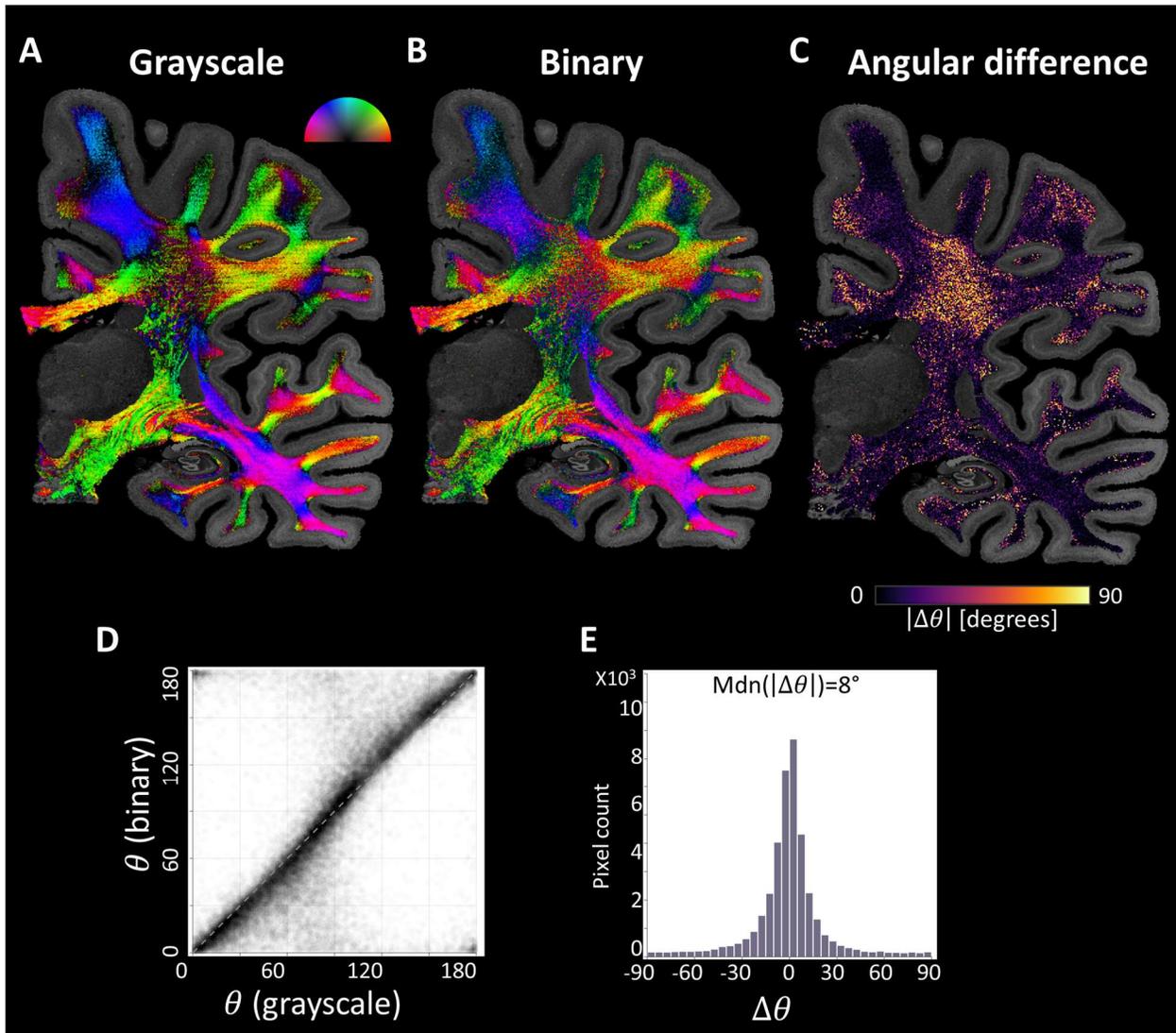
Fig. S9.

The effect of background fibrous structures on the peak orientation in an entire slice. (A-B) In-plane orientation maps in a coronal slice, calculated with 200^2 microns^2 tiles for the original grayscale **(A)** and binarized **(B)** images in which the background fibrous structures were eliminated. The peak orientation maps are largely similar, indicating that short glial cells are the main source of information in Nissl-ST. **(C)** The largest angular difference between (a) and (b) can be seen in the area of the centrum semiovale. **(D)** Scatterplot of the peak orientation in all white-matter tiles, with the orientation of the binary image plotted against the orientation of the grayscale image. **(E)** Histogram of the angular error, with a median value of 8° across white-matter tiles.
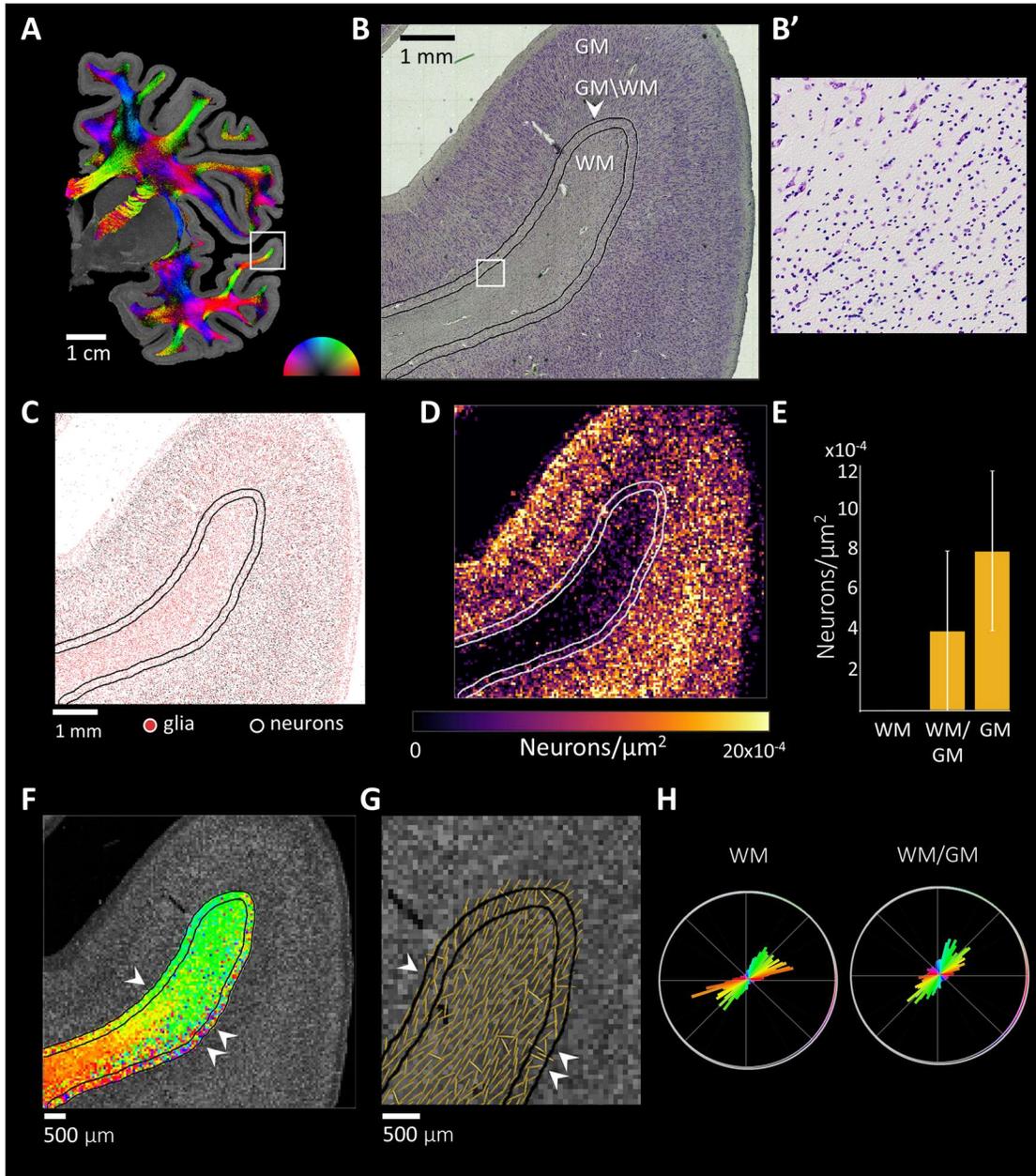
Fig. S10.
Estimating peak orientations near the cortical gray matter. (A) In-plane orientation maps in a coronal slice, calculated with 200^2 microns^2 tiles. **(B)** Nissl staining of the superior frontal gyrus (marked with a box in panel (**A**)). Histogram equalization was applied to increase the contrast between gray matter (GM) and white matter (WM). The GM/WM border has been drawn manually (outer line), and the GM/WM border region was defined as the 200-micron band at the end of the WM. (b') Magnified view of the marked regions in (b), showing the glial cells near the GM/WM border. **(C)** Automatic pixel-wise classification of glial cells (red) and neurons (black). **(D)** Heatmap of the areal density of neurons, calculated in 50^2 microns^2 tiles. Note the clear difference between WM and GM. **(E)** Bar plot of the median neuronal density in the three tissue types. Error bars represent 1 median absolute deviation from the median (MAD). **(F)** An in-plane, peak-orientation map of the WM and GM/WM border, calculated in 50^2 microns^2 tiles. Notice the continuity of orientations around the WM border: Nissl-ST typically recovers similar orientations

in the WM and in the GM/WM border (single arrowhead). In a region where the histological section cuts obliquely with respect to the convoluted cortex, we found more disordered orientations (two arrowheads). **(G)** The vector field of peak orientations in the same region, subsampled for easier visualization. In the WM, most ellipsoids point in the direction of the gyral crown. Near the GM/WM border, the ellipsoids tend to point perpendicular to the cortex. Single arrowhead represent a typical region with continuous orientations in the WM and GM/WM border. Two arrowheads mark a region with slightly more disordered orientations. **(H)** Polar histograms showing the glial rows orientation distribution functions, summarized across the two tissue types. The two histograms are largely similar, with the GM/WM histogram including more horizontal (red) and vertical (light blue) orientations.
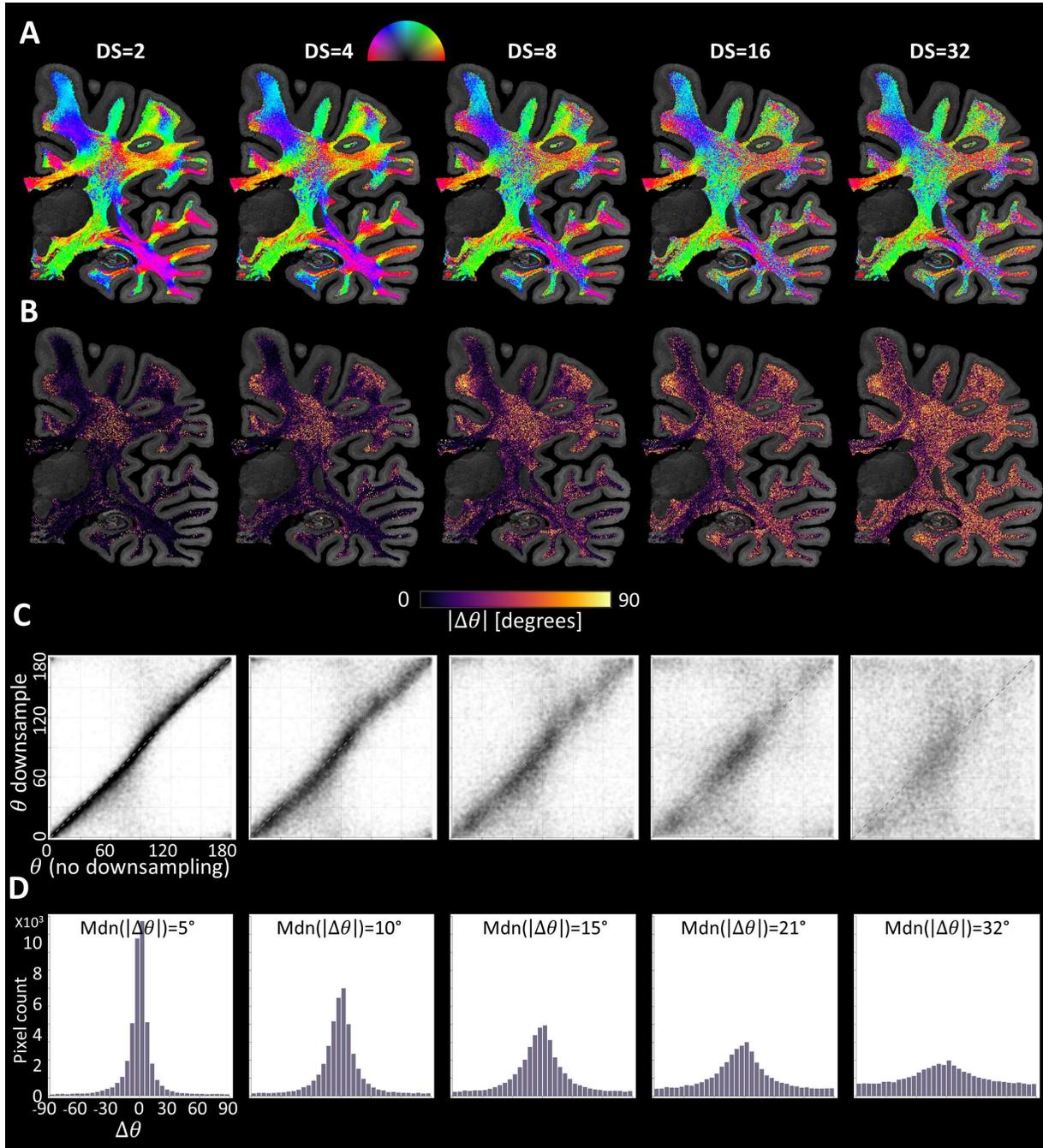
Fig. S11.

The effect of in-plane resolution on the peak orientation. A coronal slice from Dataset 1 was analyzed with different downsampling (DS) factors. **(A)** The color-coded orientation maps of each DS factor. For an easier comparison, the orientation maps were not shaded by coherence. **(B)** Maps of the angular error with respect to the native resolution. The centrum semiovale, a region of three-way fiber crossing, shows the greatest sensitivity to in-plane resolution. The angular error increases as the spatial resolution is decreased. **(C)** Scatter plots of the peak orientation in all white-matter tiles, with orientation of the downsampled image plotted against the orientation of the native resolution. **(D)** Histogram of the angular error. At a DS factor of 32 (in-plane resolution of ~20 microns), the histogram approaches a uniform distribution.
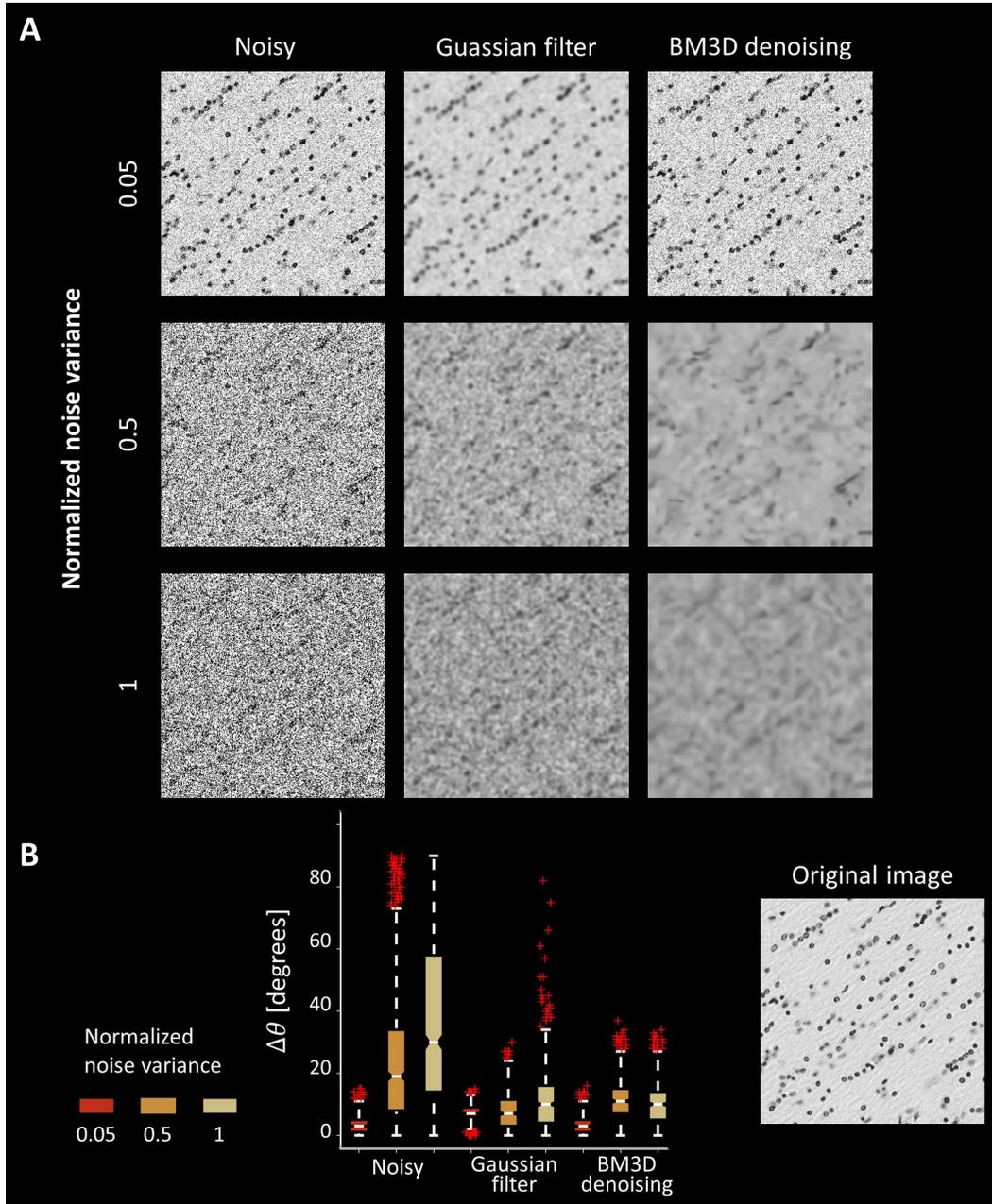
Fig. S12.
The effect of noise on the estimated peak orientation. Simulated Gaussian noise (with mean 0) was added to a 200^2 microns^2 tile from the corpus callosum. **(A)** For each of the three chosen values for normalized noise variance (0.05, 0.50 and 1.00; rows), we simulated 1,000 repeats. **Left**: An example noisy image. **Middle**: the noisy image after denoising with a median filter. **Right**: The noise image after denoising with BM3D denoising. **(B)** Boxplots showing the angular error compared with the original image, for every denoising method, and for the different noise variance values. With BM3D denoising, the median angular errors and their MAD (median absolute deviation from the median) were 2±1°, 9±3° and 8±4°, respectively. Center lines indicate median values; notches indicate 95% confidence interval for the median; box limits indicate the interquartile range (IQR; 25th-75th percentiles); whiskers extend to the most extreme data points within 1.5 IQR outside the box; outliers are represented as red crosses.
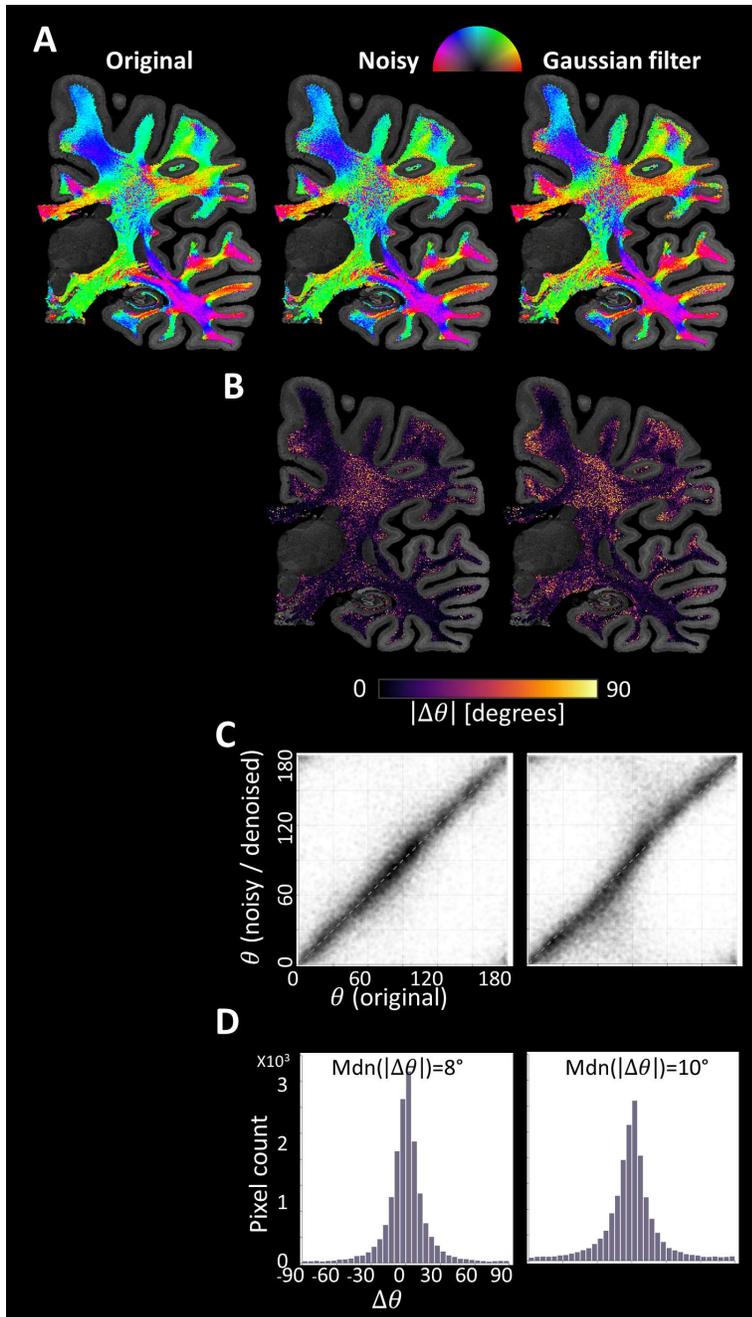
Fig. S13.
The effect of mild noise on the estimated peak orientation across a coronal slice. Simulated Gaussian noise with mean 0 and a normalized noise variance of 0.05 was added to the raw histological image. **(A)** Color-coded orientation maps of the original, noisy and denoised images. **(B)** Maps of the angular error with respect to the original image. The centrum semiovale, a region of three-way fiber crossing, shows the greatest sensitivity imaging noise. In this level of mild noise, denoising is not advantegous. **(C)** Scatter plots of the peak orientation in all white-matter tiles, with orientation of the noised (or denoised) image plotted against the orientation of the original image. **(D)** Histogram of the angular error. Denoising involves smoothing of the data, and results in a small increase in the median absolute angular error, from 8° to 10°. See Fig. S14 for the benefits of using denoising the presence of severe imaging noise.
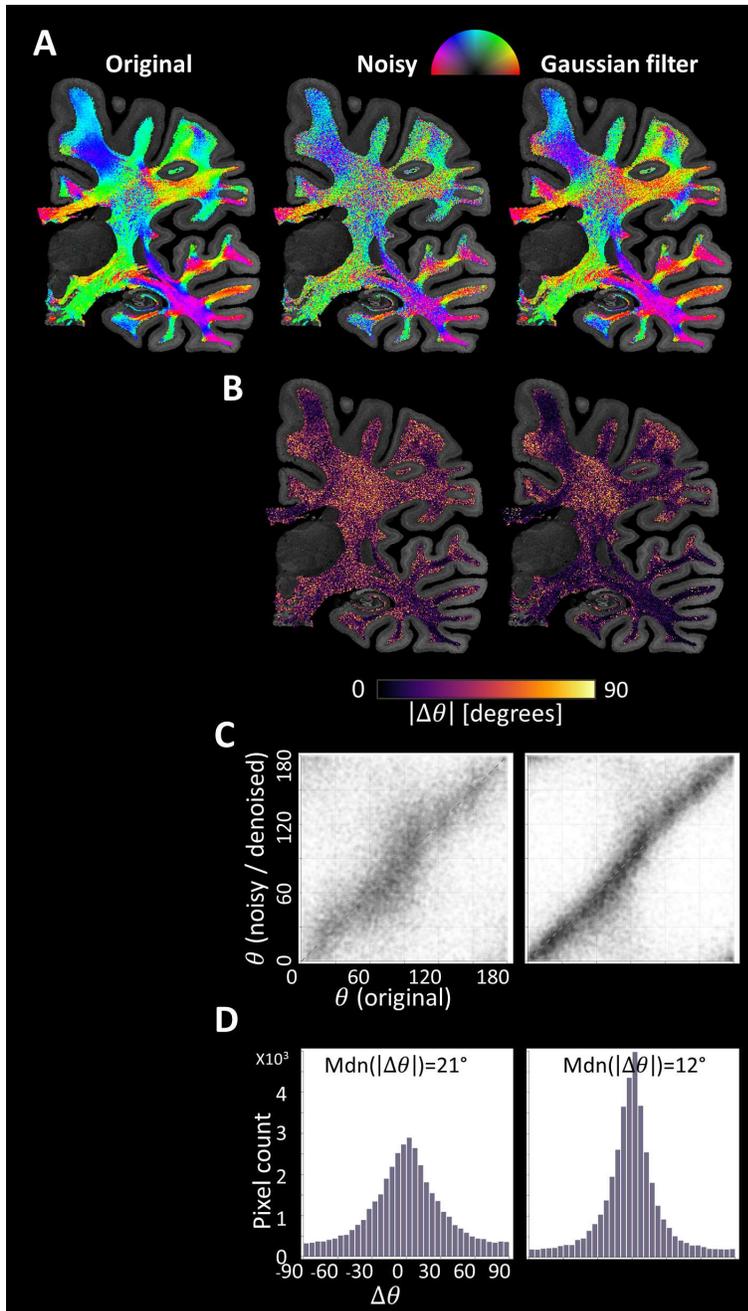
Fig. S14.
The effect of severe noise on the estimated peak orientation across a coronal slice. Simulated Gaussian noise with mean 0 and a normalized noise variance of 0.2 was added to the raw histological image. (**A**) Color-coded orientation maps of the original, noisy and denoised images. (**B**) Maps of the angular error with respect to the original image. The centrum semiovale, a region of three-way fiber crossing, shows the greatest sensitivity imaging noise. In this level of severe noise, denoising is advantageous. (**C**) Scatter plots of the peak orientation in all white-matter tiles, with orientation of the noised (or denoised) image plotted against the orientation of the original image. (**D**) Histogram of the angular error. Denoising the data under severe levels of noise results in a dramatic decrease in the median absolute angular error, from 21° to 12°.
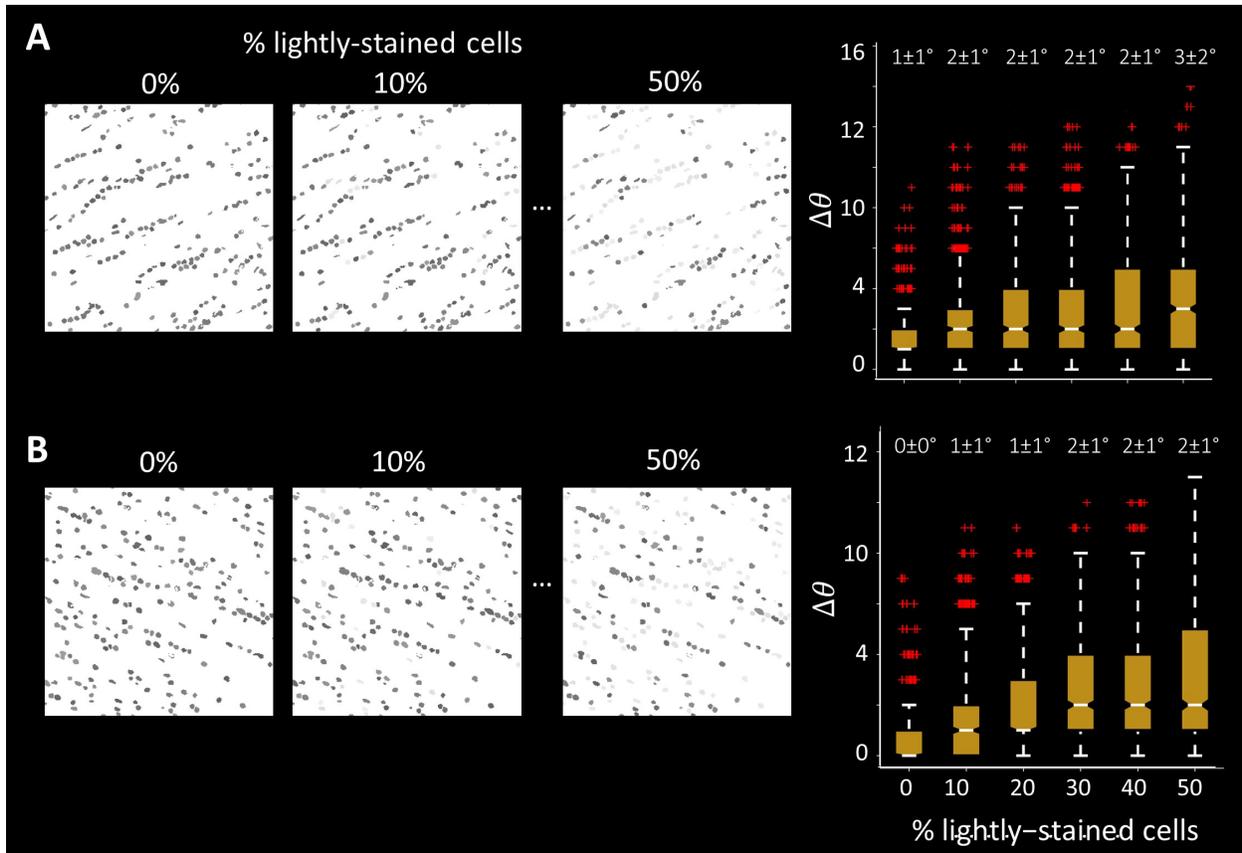
Fig. S15.

The effect of staining variability. Two 200^2 microns^2 tiles (**A** and **B**) from the corpus callosum were binarized and used to simulate variable staining. Each cell was assigned a random gray-level value (see Methods). In addition, a predetermined fraction of the cells (0,10,20,30,40 or 50%) was chosen, whose gray-level value was scaled to produce lightly stained cells. For each fraction of lightly stained cells, 1,000 images were simulated, and Nissl-ST was used to extract the peak orientation for every image. **Right**: Boxplots showing the angular error for each fraction of lightly stained cells when compared with that of the binary image with no staining variability. Even for a high faction of lightly stained cells, the median angular error remains small ($\leq 3°$). Center lines indicate median values; notches indicate 95% confidence interval for the median; box limits indicate the interquartile range (IQR; 25th-75th percentiles); whiskers extend to the most extreme data points within 1.5 IQR outside the box; outliers are represented as red crosses.
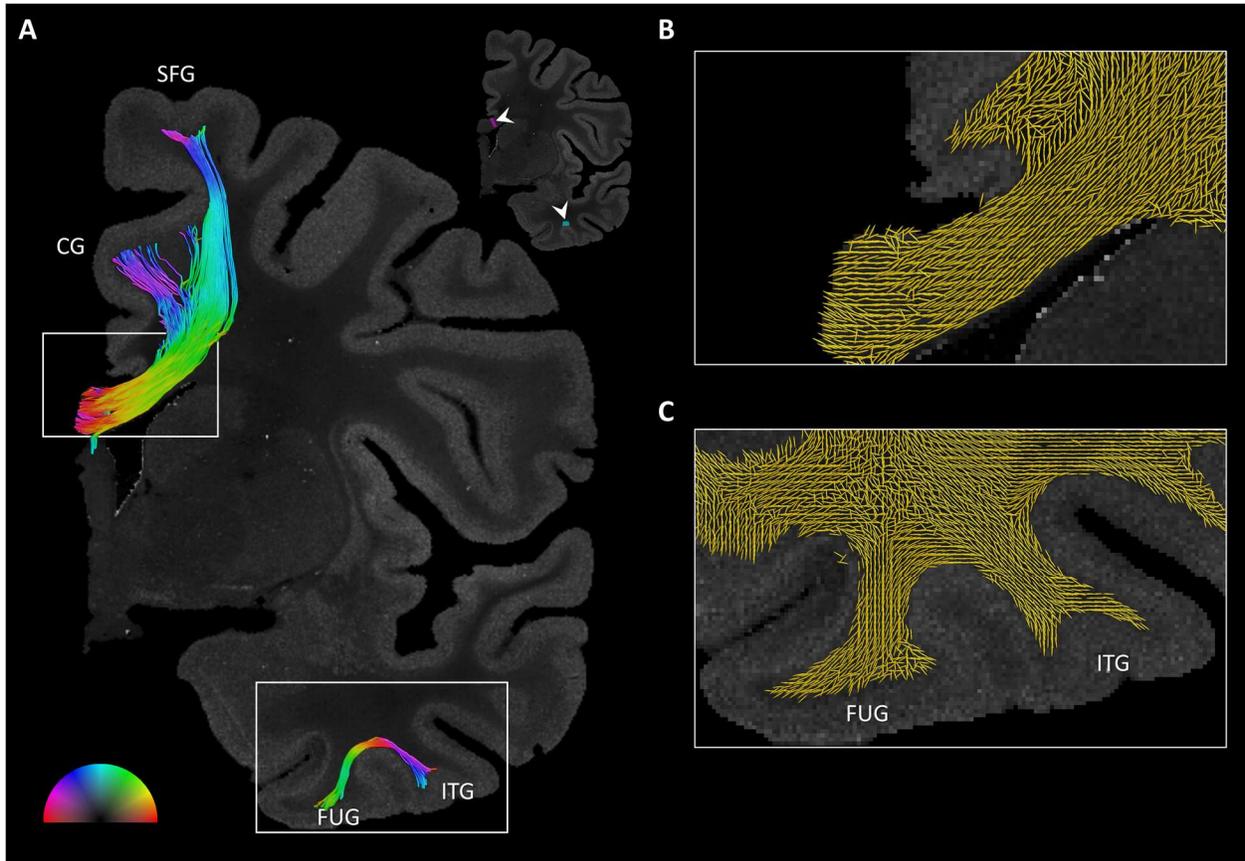
Fig. S16.

Tractography based on glial rows orientation. (A) Deterministic tractography of two fiber tracts in a coronal section of a human brain: the corpus callosum (CC) and a U-fiber around the occipitotemporal sulcus (OTS). Tractography was run on a vector field of peak orientation extracted from Nissl-ST in 200^2 microns^2 tiles, and seeded in two regions, as shown in the inset (white arrowheads). **(B-C)** Magnified views of the regions marked with boxes in (S), showing the underlying vector field visualized with ellipsoids. CG: Cingulum gyrus. FUG: Fusiform gyrus. ITG: Inferior temporal gyrus. SFG: Superior frontal gyrus.
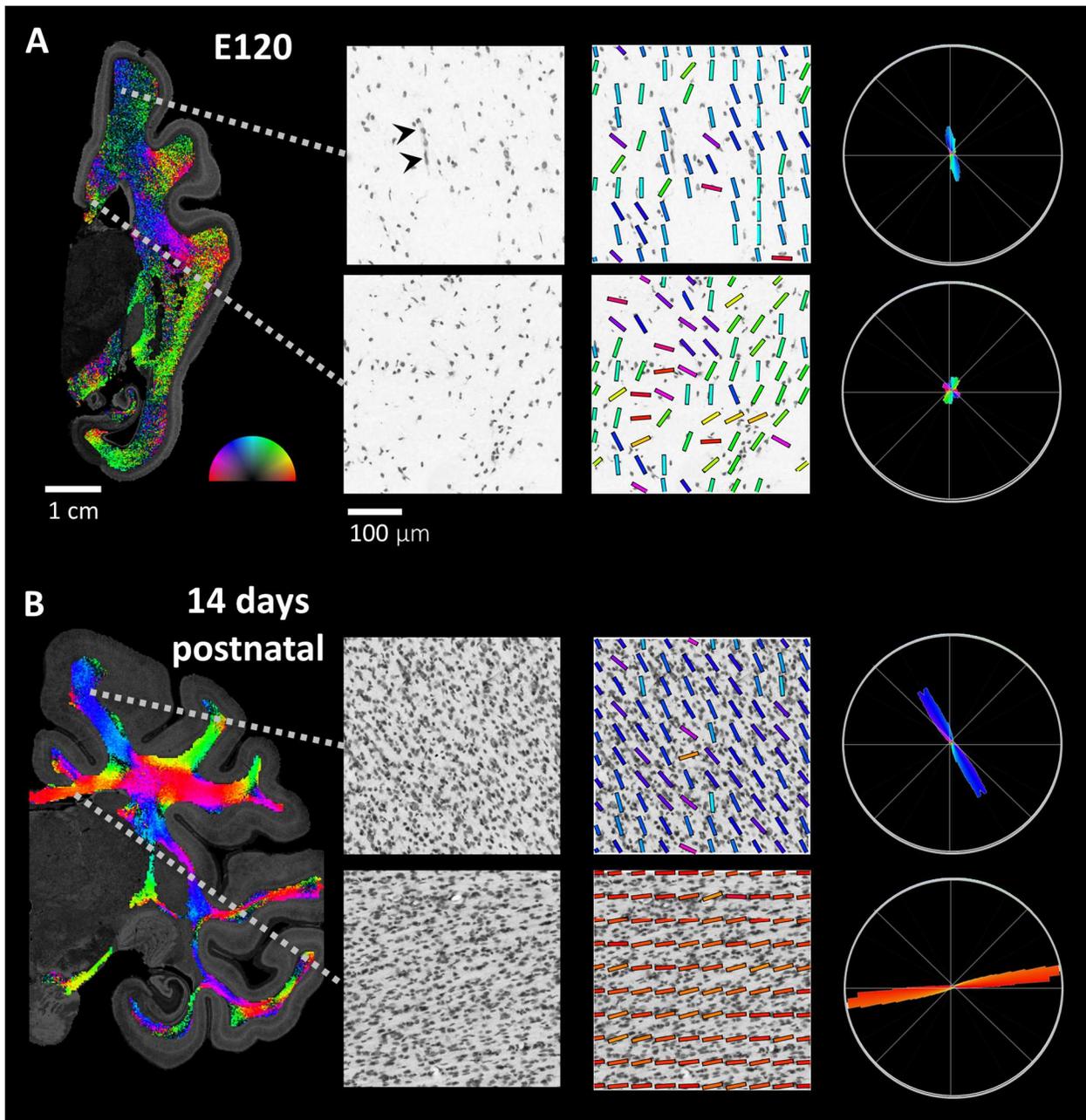
Fig. S17.
Nissl-ST reveals developmental differences in the pre- and post-natal macaque brain. In-plane orientation maps (100^2 microns^2 tiles) in coronal slices of two rhesus macaques at two developmental stages: **(A)** prenatal (120 days embryonic) and **(B)** 14 days after birth. Middle columns show typical 400^2 microns^2 tiles in the corpus callosum (top tiles per row) and the superior frontal gyrus (bottom tiles per row). Remarkably, in the prenatal stage, the density of glial cells in the white-matter is extremely low, and it is hard to detect clear glial rows. This is further indicated by the smaller and less coherent glial-row orientation distribution functions (right column), compared with those of the 14-day-old macaque. At the macroscopic level, the orientations found at the prenatal stage are not randomly distributed, but rather hold some anatomical information. This might be attributed to the effect of blood vessels (black arrowheads), which occupy a larger fraction of the stained cells at this developmental stage.
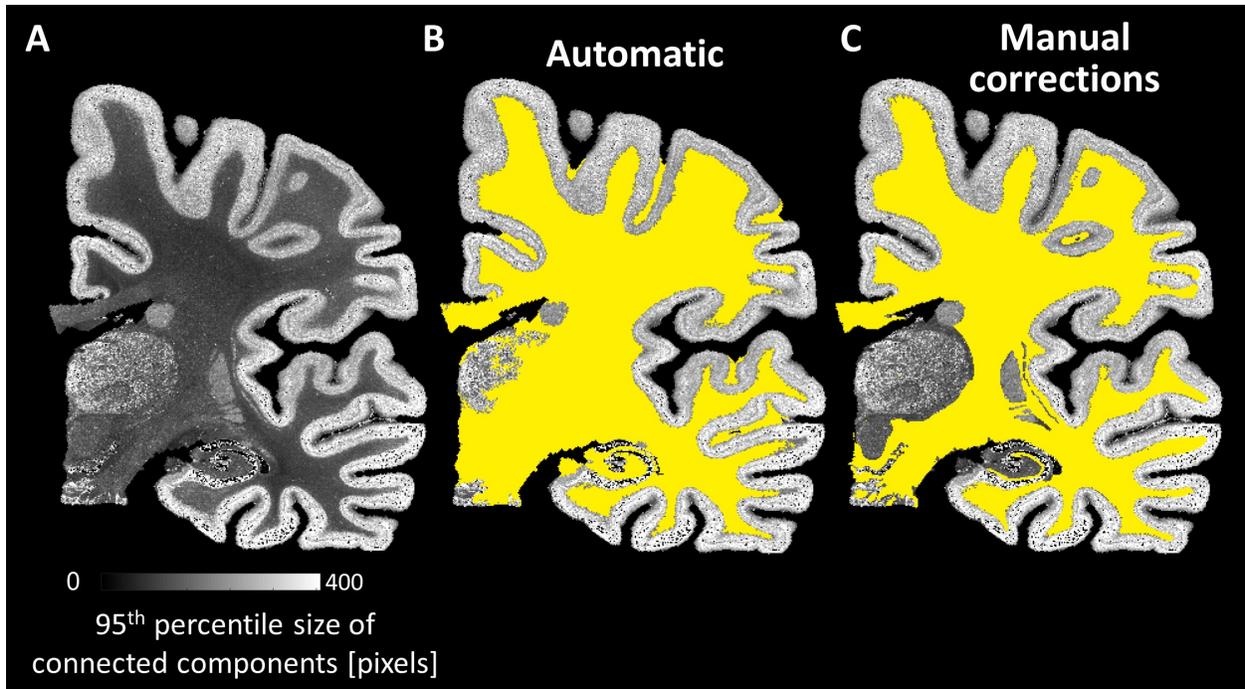
Fig. S18.
Generating a white-matter mask for visualization of in-plane orientations. (A) A coronal slice of a human brain from Dataset 1, shown with 200^2 microns^2 tiles. The gray-level value of each tile represents the 95th percentile of the size of connected components in the tile (see Methods). This yields a high contrast between gray and white matter. **(B)** An initial white-matter mask was generated automatically, by thresholding the image in (A) and filling holes. **(C)** The mask was corrected manually based on visual inspection, yielding the final white-matter mask.
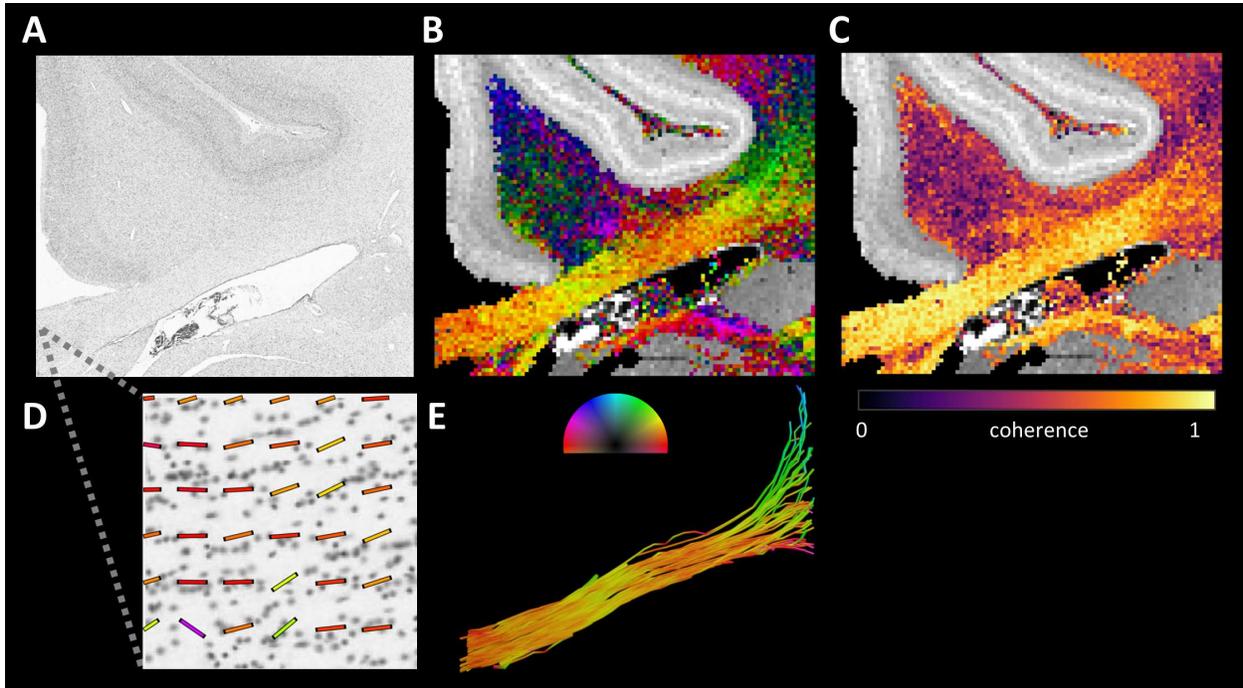
Fig. S19.
The expected outputs of running the example code. (A) The example code that we provide on GitHub downloads a section of a coronal image from a human brain (Dataset 2). The code produces a peak-orientation map calculated with 200^2 microns^2 tiles **(B)**, as well as its corresponding coherence map **(C)**. In addition, it produces a 200^2 microns^2 image tile with overlaid local orientations. **(D)** Finally, it runs tractography and visualizes the resulting corpus callosum streamlines **(E)**.

Supplementary References

47. E. G. Jones, J. M. Stone, H. J. Karten, *Ann. N. Y. Acad. Sci.* **1225**, E147 (2011).

48. J. Bigun, G. Granlund, in *First International Conference on Computer Vision, ICCV* (IEEE Computer Society, London, 1987), 433.

49. A. Seehaus et al., *Front. Neuroanat.* **9**, 1 (2015).

50. N. Otsu, , *IEEE Transactions on Systems, Man, and Cybernetics*, **9**, 62 (1979). doi:10.1109/tsmc.1979.4310076.

51. P. J. Basser, C. Pierpaoli, *J. Magn. Reson. Ser. B*. **111**, 209 (1996).

52. The GIMP Development Team, GIMP (2019).

53. M. García-Cabezas, Y. J. John, H. Barbas, B. Zikopoulos, *Front. Neuroanat.* **10** (2016), doi:10.3389/fnana.2016.00107.

54. S. Berg et al., *Nat. Methods*. **16**, 1226 (2019).

55. O. Dietrich, J. G. Raya, S. B. Reeder, M. F. Reiser, S. O. Schoenberg, *J. Magn. Reson. Imaging*. **26**, 375 (2007).

56. Y. Makinen, L. Azzari, A. Foi, *Proc. Int. Conf. Image Process. ICIP*., 185 (2019).

57. J. D. Yeatman, R. F. Dougherty, N. J. Myall, B. A. Wandell, H. M. Feldman, *PLoS One*. **7**, e49790 (2012).

58. D. C. Van Essen et al., *Neuroimage*. **62**, 2222 (2012).

59. M. F. Glasser et al., *Neuroimage*. **80**, 105 (2013).

60. J.D. Tournier et al., *Neuroimage*, 116137 (2019).

61. J. D. Tournier, F. Calamante, A. Connelly, *Neuroimage*. **35**, 1459 (2007).

62. R. E. Smith, J. Tournier, F. Calamante, A. Connelly, *Neuroimage*. **67**, 298 (2013).

63. D. Raffelt et al., *Neuroimage*. **59**, 3976 (2012).

64. H. Nonaka, M. Akima, T. Hatori, T. Nagayama, Z. Zhang, F. Ihara, *J. Neuropathol. Exp. Neurol.* **62**, 154 (2003).

65. T. Kubíková, P. Kochová, P. Tomášek, K. Witter, Z. Tonar, *J. Chem. Neuroanat.* **88**, 22 (2018).

66. C. S. von Bartheld, J. Bahney, S. Herculano-Houzel, *J. Comp. Neurol.* **524**, 3865 (2016).

67. S. Jbabdi, H. Johansen-Berg, *Brain Connect.* **1**, 169 (2011).

68. F. D. S. Requejo, P. L. Laguna, A. Beyh, S. Williams, M. Catani, F. Dell'Acqua, in *Organization for Human Brain Mapping* (Vancouver, 2017), 2050.

69. A. Lee, *Wiley Interdiscip. Rev. Comput. Stat.* **2**, 477 (2010).

70. K. Wagstyl et al., *PLOS Biol.* **18**, e3000678 (2020).